Reactor-based Neutrino Oscillation Experiments

Carlo Bemporad[1], Giorgio Gratta[2], and Petr Vogel[3]

[1] INFN and University of Pisa, Pisa, Italy
[2] Physics Department, Stanford University, Stanford CA 94305, USA
[3] Physics Department, California Institute of Technology, Pasadena, CA 91125, USA

The status of neutrino oscillation searches employing nuclear reactors as sources is reviewed. This technique, a direct continuation of the experiments that proved the existence of neutrinos, is today an essential tool in investigating the indications of oscillations found in studying neutrinos produced in the sun and in the earth's atmosphere. The low-energy of the reactor $\bar{\nu}_e$ makes them an ideal tool to explore oscillations with small mass differences and relatively large mixing angles. In the last several years the determination of the reactor anti-neutrino flux and spectrum has reached a high degree of accuracy. Hence measurements of these quantities at a given distance L can be readily compared with the expectation at $L = 0$, thus testing $\bar{\nu}_e$ disappearance. While two experiments, Chooz and Palo Verde, with baselines of about 1 km and thus sensitive to the neutrino mass differences associated with the atmospheric neutrino anomaly, have collected data and published results recently, an ambitious project with a baseline of more than 100 km, KamLAND, is preparing to take data. This ultimate reactor experiment will have a sensitivity sufficient to explore part of the oscillation phase space relevant to solar neutrino scenarios. It is the only envisioned experiment with a terrestrial source of neutrinos capable of addressing the solar neutrino puzzle.

I. INTRODUCTION

Neutrinos have the distinction of being the first elementary particle whose existence was predicted by a theorist in order to explain seemingly unrelated phenomena*. Pauli made such prediction in 1930 in his famous letter in order to explain the continuous electron energy distribution in nuclear beta decay. It became immediately clear that neutrinos will be difficult to observe, because the corresponding cross sections are so tiny. But in a series of experiments in 1953-59 Reines and Cowan (1953, 1959) were able to prove convincingly that electron anti-neutrinos from nuclear reactors are able to cause the inverse neutron beta decay, $\bar{\nu}_e + p \rightarrow e^+ + n$, and hence that they are real particles. Shortly afterwards, in 1962, the separate identity of the muon neutrinos, ν_μ, was demonstrated (Danby *et al.* 1962). Another decade later, in 1975, the τ lepton was discovered (Perl *et al.* 1975) and the observation of its decay properties implied the existence of the third neutrino, ν_τ, that was directly observed only very recently (Kodama *et al.* 2001). Precise measurements of the decay width of the Z have shown that just three neutrino flavors (2.994 ± 0.012 from the combined fit to all LEP data (Groom *et al.* 2000)) participate in the weak interactions (at least for neutrinos with masses less than $1/2M_Z$).

Phenomenologically, it is obvious that neutrinos of each flavor are either massless or at least many orders of magnitude lighter than the corresponding charged leptons with which they form the weak interaction doublets. Based on these empirical facts, the Standard Electroweak Model *postulates* that all neutrinos are massless, and consequently have conserved helicity (which is the same as chirality in this case) and that the separate lepton numbers for electron, muon, and tau flavors are conserved. Challenging this postulate of the vanishing neutrino mass has recently become a central issue in many disciplines of fundamental science, including particle and nuclear physics, cosmology, and astrophysics. The present review is devoted to one particular aspect of this broad effort.

Ironically, while our knowledge of intrinsic neutrino properties remains quite poor, these particles have been

*For early development in neutrino physics see, for example, Chapter 1 in Winter (1981).

used as tools to understand other phenomena. The tradition of underground neutrino detectors began thirty years ago when Davis and his collaborators were first able to detect neutrinos from the Sun. (For the description of the history of solar neutrino research see (Bahcall 1989).) This was, and together with the other experimental observations of the solar neutrinos still is, the only clear proof that the basic energy generation in stars is understood. The birth of neutrino astronomy can be associated with the observation of the neutrino burst from the supernova 1987A. Neutrino-induced reactions played an important role in establishing what is now known as the Standard Model of electroweak interactions when in 1973 the neutral currents were discovered via the observation of the $\nu_\mu + e \to \nu_\mu + e$ scattering as well as the neutral current scattering of neutrinos on nucleons. Finally, neutrinos have been extensively used in deep inelastic scattering experiments at CERN and FNAL, exploring the quark structure of nucleons.

The main problem in neutrino physics today is the question whether neutrinos, like all charged fermions, have a mass[†]. Since direct kinematic tests of neutrino mass lack at present the required sensitivity, the recent hints for neutrino mass are indirect, based on the phenomenon of neutrino oscillations. If neutrinos are massive particles which behave in analogy to quarks, the states with a definite mass (i.e., the "mass eigenstates" which propagate as plane waves in vacuum) are not necessarily the partners of the charged leptons that couple to the vector bosons $W^\pm$ in doublets (i.e., the weak or flavor eigenstates)

$$\begin{pmatrix} \nu_{\mathrm{e}} \\ \mathrm{e}^- \end{pmatrix} , \begin{pmatrix} \nu_\mu \\ \mu^- \end{pmatrix} , \begin{pmatrix} \nu_\tau \\ \tau^- \end{pmatrix} . \quad (1)$$

The weak eigenstates $|\nu_l\rangle$ will be in such a case linear superpositions of the mass eigenstates $|\nu_i\rangle$

$$|\nu_l\rangle = \sum_i U_{l,i} |\nu_i\rangle , \quad (2)$$

where the coefficients $U_{l,i}$ form the leptonic mixing matrix. If we assume that only three neutrinos can contribute in the Eq.(2) above, then U is a unitary 3×3 matrix[‡].

If Eq.(2) is valid, we encounter the phenomenon of neutrino oscillations in which a neutrino that was initially in the weak eigenstate l can be spontaneously transformed, at least in part, into another weak eigenstate neutrino of flavor l'. (The idea of oscillations was discussed early on by Pontecorvo (1958, 1967) and by Maki, Nakagawa and Sakata (1962).)

To see how that transformation happens, recall that the mass eigenstate $|\nu_i\rangle$ propagates according to the expression

$$|\nu_i(t)\rangle = e^{-i(E_i t - p_i L)} |\nu_i(0)\rangle \simeq e^{-i(m_i^2/2E)L} |\nu_i(0)\rangle , \quad (3)$$

where L is the flight path and in the last expression we assumed that the laboratory momenta and energies are much larger than the neutrino rest masses m_i. Let us consider now the propagation of a neutrino which was created at $L = 0$ as a weak eigenstate $|\nu_l\rangle$. At a distance L this state is described by

$$\begin{aligned} |\nu_l(L)\rangle &\simeq \sum_i U_{l,i} e^{-i(m_i^2/2E)L} |\nu_i\rangle \\ &\simeq \sum_{l'} \sum_i U_{l,i} e^{-i(m_i^2/2E)L} U^*_{l',i} |\nu_{l'}\rangle . \quad (4) \end{aligned}$$

In the last expression we used the inverse transformation to Eq.(2), i.e., from the mass eigenstates back to the weak eigenstates. This step must be taken since the only way one can detect neutrinos is through their weak interactions. And in order to detect the neutrino flavor we have to use the charged current weak interactions, characterized by the production of the charged leptons $|l'\rangle$.

Thus, the neutrino of flavor l acquired components corresponding to other flavors l'. This is a purely quantum mechanical effect, a consequence of the coherence in the superposition of states in Eq.(2). The probability that the "transition" $l \to l'$ happens at L is obviously

$$P(\nu_l \to \nu_{l'}) = |\sum_i U_{l,i} U^*_{l',i} e^{-i(m_i^2/2E)L}|^2$$

$$= \sum_i |U_{li} U^*_{l'i}|^2 + \Re \sum_i \sum_{j \neq i} U_{li} U^*_{l'i} U^*_{lj} U_{l'j} e^{i \frac{|m_i^2 - m_j^2| L}{2p}} . \quad (5)$$

This is an oscillating function of the distance L. The oscillation length depends on the differences of the neutrino mass squares, $|m_i^2 - m_j^2|$, and the oscillation amplitude depends on the mixing matrix U.

The necessary and sufficient conditions for the existence of neutrino oscillations is then the nonvanishing value of at least one neutrino mass m_i and the nonvanishing value of at least one nondiagonal matrix element of the mixing matrix U. If these conditions are fulfilled, the individual lepton flavor numbers (electron, muon, tau) are no longer conserved.

There is no fundamental theory which would allow us to deduce the parameters describing the mixing matrix U

[†]For an up-to-date discussion of the neutrino masses and the relevant experiments see (Fisher, Kayser, and McFarland 1999) and (Zuber 1998).

[‡]Sometimes more than 3 mass eigenstates are considered. The additional neutrinos must be sterile or heavy, i.e., they must not participate in weak interactions so that the constraint from the invisible width of the Z boson is obeyed.

and the mass differences Δm^2_{ij}. These unknown parameters must be determined empirically, by various neutrino oscillation experiments. Such analysis is often performed in a simplified way by assuming that only two neutrino flavors mix, e.g. e and μ. The mixing matrix U then depends only on one mixing angle θ, and the oscillation probability, Eq. (5), is also simplified

$$U = \begin{pmatrix} \cos\theta & \sin\theta \\ -\sin\theta & \cos\theta \end{pmatrix} ,$$
$$P(\nu_{\rm e} \to \nu_\mu, L) = \sin^2 2\theta \sin^2(\Delta m^2 L/4E) \ . \quad (6)$$

Here $\Delta m^2 \equiv m_1^2 - m_2^2$, and we assume, as before, that the neutrinos are ultrarelativistic. The probability that $\nu_{\rm e}$ remains $\nu_{\rm e}$ is obviously

$$P(\nu_{\rm e} \to \nu_{\rm e}, L) = 1 - P(\nu_{\rm e} \to \nu_\mu, L). \quad (7)$$

In this two-flavor scenario the oscillation amplitude is $\sin^2 2\theta$ which vanishes if $\theta = 0$ or $90°$ and is maximum if $\theta = 45°$. The oscillation length is

$$L_{osc} = 2\pi \frac{2E_\nu}{\Delta m^2} = \frac{2.48 E_\nu({\rm MeV})}{\Delta m^2({\rm eV}^2)} {\rm meters} \ . \quad (8)$$

To test for oscillations, one can perform either an *appearance* search in which one looks for a new neutrino flavor (i.e., the deviations of $P(\nu_{\rm e} \to \nu_\mu, L)$ from zero), or a *disappearance* test in which one looks for a change in the flux normalization (i.e., the deviation of $P(\nu_{\rm e} \to \nu_{\rm e}, L)$ from unity). In either case, tests performed at distance L are only sensitive to the values of Δm^2 for which $L \geq O(L_{osc})$. Or, in other words, neutrino oscillations are observable only when $\Delta m^2 L/E \sim O(1)$.

So far we have considered only propagation of neutrinos in a vacuum. When neutrinos propagate in matter, such as in the solar interior, the oscillation pattern may be modified. This happens because electron neutrinos can forward scatter on electrons by charged current interactions, and other neutrino flavors cannot. Under favorable circumstances a resonance enhancement of the oscillation amplitude, the so-called Mikheyev-Smirnov-Wolfenstein (MSW) effect (Wolfenstein 1979, 1980) and (Mikheyev and Smirnov 1986a, 1986b), can take place. Analogous matter induced oscillations can distinguish the hypothetical sterile neutrinos, which have no weak interactions at all, and the ν_μ or ν_τ neutrinos which interact with matter (electrons and quarks) by the neutral current weak interaction. Neither of these kinds of matter effects is relevant for reactor neutrinos.

For completeness, it is worthwhile to mention here two other issues important in the study of the neutrino intrinsic properties. One of them deals with the charge conjugation properties of the neutrinos. Unlike the charged leptons, which are Dirac particles, with distinct antiparticles, neutrinos can be either Dirac or Majorana particles. In the latter case of truly neutral neutrinos, there is no distinction between the neutrinos and their antiparticles, and even the total lepton number is not conserved. In order to decide between these two possibilities, one has to look for processes that violate the total lepton number, such as the neutrinoless double beta decay. Other processes of this kind, like the $\nu_e \to \bar{\nu}_e$ oscillations (e.g. in the present context the emission of ν_e from the nuclear reactor) are typically kinematically supressed, and their observation is unlikely in forseeable future. The difference between the Dirac and Majorana neutrinos, while of fundamental importance, does not influence the results of the reactor oscillation searches described below.

The other issue worth mentioning is the possibility of the T or CP violation in neutrino oscillations (Cabibbo 1978 and Barger, Whisnant and Phillips 1980). In order to establish violation of T or CP one would have to show that

$$P(\nu_{\ell'} \to \nu_\ell) \neq P(\bar{\nu}_{\ell'} \to \bar{\nu}_\ell) \ , \quad (9)$$

i.e., that for example the probability of ν_μ oscillating into ν_e is different from the probability of $\bar{\nu}_\mu$ oscillating into $\bar{\nu}_e$.

For the usual case of three neutrino flavors, one can parametrize the lepton mixing matrix in terms of the three angles $\theta_1 = \theta_{13}$, $\theta_2 = \theta_{23}$, and $\theta_3 = \theta_{12}$ and the CP violating phase δ.

$$\begin{pmatrix} \nu_e \\ \nu_\mu \\ \nu_\tau \end{pmatrix} = \quad (10)$$
$$\begin{pmatrix} c_1 c_3 & c_1 s_3 & s_1 e^{-i\delta} \\ -c_2 s_3 - s_1 s_2 c_3 e^{i\delta} & c_2 c_3 - s_1 s_2 s_3 e^{i\delta} & c_1 s_2 \\ s_2 s_3 - s_1 c_2 c_3 e^{i\delta} & -s_2 c_3 - s_1 c_2 s_3 e^{i\delta} & c_1 c_2 \end{pmatrix} \begin{pmatrix} \nu_1 \\ \nu_2 \\ \nu_3 \end{pmatrix}$$

where e.g. $c_1 = \cos\theta_1$ and $s_1 = \sin\theta_1$, etc.

The magnitude of the T or CP violation is characterized by the differences

$$P(\bar{\mu} \to \bar{e}) - P(\mu \to e) = -[P(\bar{\mu} \to \bar{\tau}) - P(\mu \to \tau)] =$$
$$P(e \to \tau) - P(\bar{e} \to \bar{\tau}) =$$
$$-4c_1^2 s_1 c_2 s_2 c_3 s_3 \sin\delta [\sin\Delta_{12} + \sin\Delta_{23} + \sin\Delta_{31}] \ , \quad (11)$$

where $\Delta_{ij} = (m_i^2 - m_j^2) \times L/2E$.

Thus, the size of the effect is the same in all three channels, and CP violation is observable only if all three masses are different (i.e., nondegenerate), and all three angles are nonvanishing. As will be shown below, reactor experiments constrain the angle θ_1 (or θ_{13}), to be small ($\sin^2 2\theta_{13} \leq 0.1$). If that mixing angle vanishes exactly, no CP violation is observable in the lepton sector, independently of the value of the CP violating phase δ. To further improve the sensitivity to $\sin^2 2\theta_{13}$ is, therefore, a matter of utmost importance.

II. PHYSICS MOTIVATION OF MODERN EXPERIMENTS

Numerous searches for neutrino oscillations were performed during the last two decades using nuclear reactors as well as particle accelerators as sources. Since most of them have not observed evidence for neutrino oscillations, their results are usually based on the simplified two neutrino mixing scenario and presented as an "exclusion plot", i.e., based on them certain ranges of the parameters Δm^2 and $\sin^2 2\theta$ can be excluded from further considerations as shown in Figure 1. However, at the present time there are three groups of measurements that suggest the existence of neutrino oscillations. (And, at the same time, the parameter ranges suggested by them are not excluded.) Only these *positive* results will be briefly discussed here, other experiments are listed in the Review of Particle Properties (Groom *et al.* 2000).

A. Experimental indications for neutrino oscillations

The most prominent group of measurements which are commonly interpreted as evidence for neutrino oscillations are often referred to as the "atmospheric neutrino anomaly" (Kajita and Totsuka 2001). Primary cosmic rays impinging on the nitrogen and oxygen nuclei at the top of the earth's atmosphere produce mostly pions, which subsequently decay via the chain $\pi^- \to \mu^- \bar{\nu}_\mu, \mu^- \to e^- \bar{\nu}_e \nu_\mu$ (and the analogous chain with π^+ etc.). At sufficiently low energy, when such chains can fully develop, the resulting atmospheric neutrinos therefore are expected to follow the $\nu_\mu : \nu_e = 2 : 1$ ratio, which is essentially independent of the details of the complicated process that created them. In addition, in an underground detector, one can deduce the direction of the incoming neutrinos from the direction of the leptons (e and μ) created by the charged current interactions. Again, one is reasonably confident that this zenith angle distribution can be accurately predicted. If the ν_μ and/or ν_e neutrinos oscillate, one expects deviations from the 2:1 ratio mentioned above. Also, since the zenith angle is simply related to the neutrino path length, one expects deviations from the expected zenith angle dependence of the lepton yield.

Both signatures of neutrino oscillations were in fact observed. The ν_μ/ν_e ratio is noticeably smaller, only about 60%, than the expected value. This result has been confirmed in four detectors thus far. The anomalous zenith angle dependence was first observed in Kamiokande, and has been now confirmed, with much better statistical significance, by SuperKamiokande (Kajita and Totsuka 2001, Fukuda 1998, Fukuda 2000). If these effects indeed signify neutrino oscillations (and we do not know of another viable explanation) then the corresponding mixing angle is large, $\sin^2 2\theta \approx 1$, and the value of the mass parameter Δm^2 is in the range 10^{-2} - 10^{-3} eV^2. While the preferred scenario at present involves $\nu_\mu \to \nu_\tau$ oscillations, it is not clear that $\nu_\mu \to \nu_e$ oscillations are fully excluded.

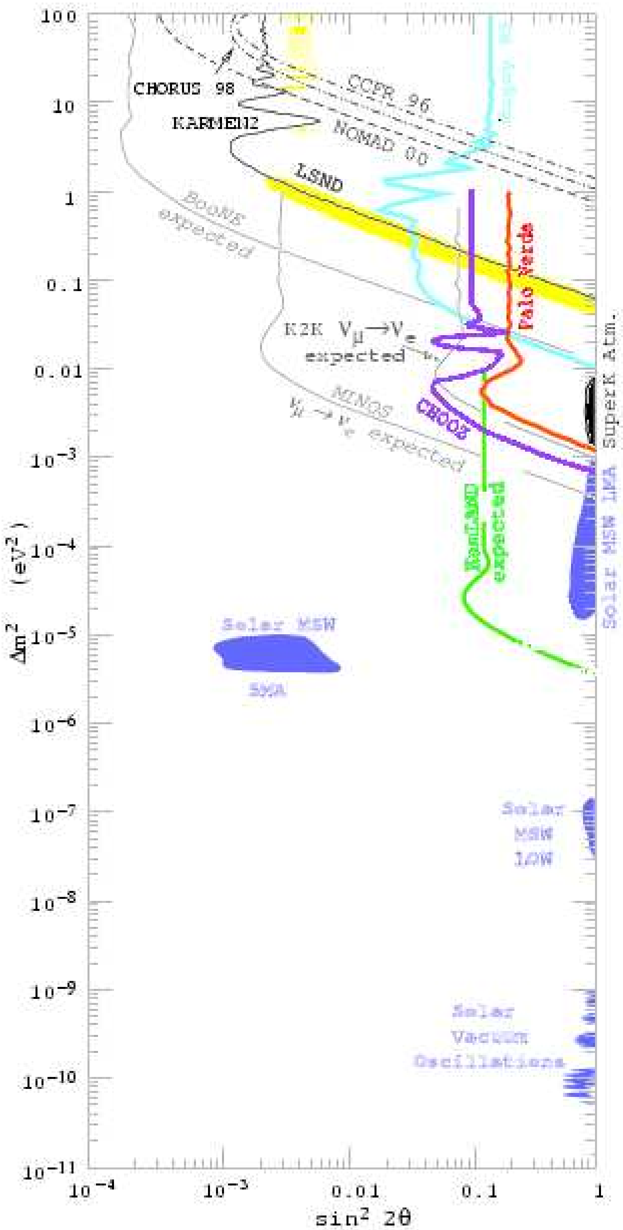

FIG. 1. Phase-space for neutrino oscillations. The existing limits on $\nu_e - \nu_\mu$ are compared with current and future experiments and the regions obtained by interpreting the solar, atmospheric and LSND neutrino anomalies as due to oscillations (some of these effects are not necessarily $\nu_e - \nu_\mu$ oscillations.) The MSW mechanism is used in plotting some of the solar neutrino regions. The sensitivity of reactor experiments is the same for $\nu_e - \nu_\tau$ oscillations. Limits are at 90% CL.

The second set of measurements that can be interpreted as evidence for neutrino oscillations deals with the "missing" solar neutrinos (Kirsten 2000, latest results in Fukuda 2001 and in particular in Ahmad 2001). The Sun produces an intense flux of electron neutrinos as a byproduct of the fusion reactions which generate solar power. It is believed that the solar structure is understood sufficiently well so that the flux and energy spectrum of the neutrinos can be confidently predicted. The solar neutrino fluxes have been measured in six experiments so far. All of them report a deficit, i.e., the measured flux is less than the expected one. Moreover, the reduction depends on the neutrino energy, inferred experimentally from the thresholds of the individual detectors. The only viable explanation of the deficit appears to be neutrino oscillation (ν_e disappearance). The hypothesis that solar ν_e indeed oscillate into 'active' neutrinos that scatter on electrons via the neutral current weak interaction is supported, at the 3 σ level, by combining the pure charged current measurements of SNO (Ahmad 2001) with the charged + neutral current measurement of Super-Kamiokanke (Fukuda 2001).

By contrast to the attempts to explain the deficit by modification of the solar model, which are unsuccessful, all existing data can be simply and elegantly explained by invoking neutrino mass. In particular, the solution based on the MSW effect offers the most popular scenario. Treating the problem in the two-flavor framework explained above, one arrives at several isolated islands in the Δm^2 – $\sin^2 2\theta$ plane. Two solutions correspond to $\Delta m^2 \approx 10^{-5}$ eV^2. One of them ("small mixing angle" or SMA) has $\sin^2 2\theta \approx 10^{-2}$, while the other one ("large mixing angle" or LMA) has $\sin^2 2\theta \geq 0.5$. This latter solution, currently giving the best fit to the data, spans an interval of Δm^2 extending up to 10^{-4} eV^2. The other possibilities have large mixing angles and $\Delta m^2 \approx 10^{-7}$ eV^2 (LOW) or $\Delta m^2 \approx 10^{-10}$ eV^2 (vacuum).

Finally, the only indication for oscillations involving man-made neutrinos comes from the LSND experiment which finds evidence for the $\bar{\nu}_\mu \rightarrow \bar{\nu}_e$ and, with more limited statistics, also for $\nu_\mu \rightarrow \nu_e$ (Athanassopoulos *et al.* 1995, 1996, 1998). The former channel uses neutrinos from the pion and muon decay at rest, with energies less than $m_\mu/2$. The latter channel uses neutrinos from the pion decay in flight which have somewhat higher energies. These are appearance experiments; the observed signal should be absent if neutrinos do not oscillate. The well determined quantity is the oscillation probability, which has the value of about 3×10^{-3}. This result has not been independently confirmed. An analogous experiment which also uses the neutrinos from the pion and muon decay at rest, KARMEN (Armbruster *et al.* 1998, Eitel 2000), found no evidence for the $\bar{\nu}_\mu \rightarrow \bar{\nu}_e$ oscillations. However, the parameter space compatible with the LSND signal is not fully excluded by KARMEN.

As we can see from this brief discussion, the last decade brought us a number of clues. With the exception of the LSND signal, they all came from measurements involving neutrinos produced by natural sources outside of our control. A number of new experiments has been performed or are in various stages of planning in order to investigate further these tantalizing effects. Reactor experiments play an all-important role in this quest, owing to their unique ability to investigate very small neutrino-mass differences.

Like in many other aspects of neutrino physics there is a fundamental difference between the past reactor oscillation experiments[§] and the more recent experiments with baselines of 1 km or more: experiments in this latter category are designed to further investigate, in a controlled environment with man-made neutrinos, particular regions of the oscillation parameter space where there are indications for oscillations from other experiments. Hence the results from the new generation of reactor $\bar{\nu}_e$ detectors directly impact our understanding of the neutrino mixing matrix.

B. Reactor versus accelerator-based oscillation experiments

Nuclear reactors produce isotropically $\bar{\nu}_e$ in the β decay of the neutron-rich fission fragments. All detectors optimized for oscillation searches take advantage of the relatively large cross-section and specific signature of the inverse-β-decay reaction $\bar{\nu}_e + p \rightarrow n + e^+$. Such cross-section is shown in Figure 2 as function of the neutrino energy along with the neutrino flux at the reactor and the resulting interaction rate in a detector. We note here that the detection reaction has a threshold of about 1.8 MeV. Many of the merits and limitations of reactor-based experiments can be understood observing that the energy of $\bar{\nu}_e$ is rather low, in the few-MeV range. It directly follows that reactor-based experiments can only be of $\bar{\nu}_e$ -disappearance type since the neutrino "beam" does not have sufficient energy to produce muons (or taus) and the neutral-current reactions of the "oscillated" $\bar{\nu}_\mu$ or $\bar{\nu}_\tau$ have too low cross-section and are un-distinguishable from the many backgrounds present. This first limitation makes reactor-based experiments well suited only for investigating relatively large mixing angles. In practice experiments have reported mixing sensitivities around 10% at large Δm^2 (although the proposal for a very ambitious experiment with sensitivity better than 2% at a particular Δm^2 will be discussed later). The second limitation of reactor-based oscillation searches derives from the

[§]For a general discussion of short-baseline reactor experiments see Boehm and Vogel 1992 and Boehm 2001; for the individual experiments see Kwon *et al.* 1981, Zacek *et al.* 1986, Achkar 1992, Achkar *et al.* 1995 and 1996, Vidyakin *et al.* 1994, Alfonin *et al.* 1998.

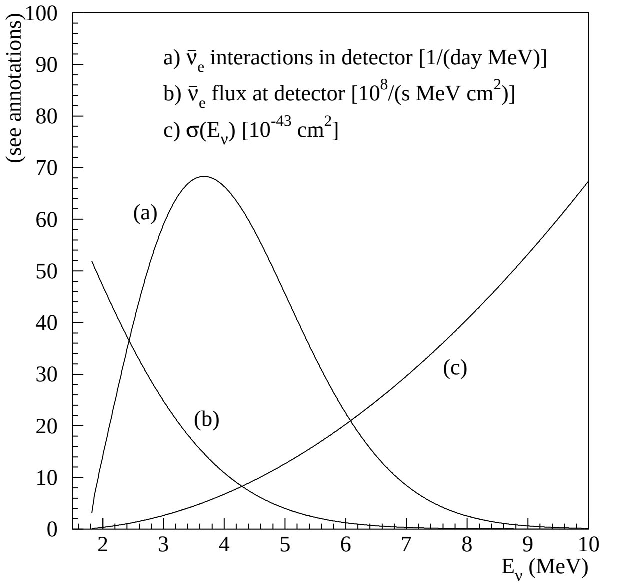

FIG. 2. Reactor $\bar{\nu}_e$ flux, inverse beta decay cross section, and $\bar{\nu}_e$ interaction spectrum at a detector based on such reaction.

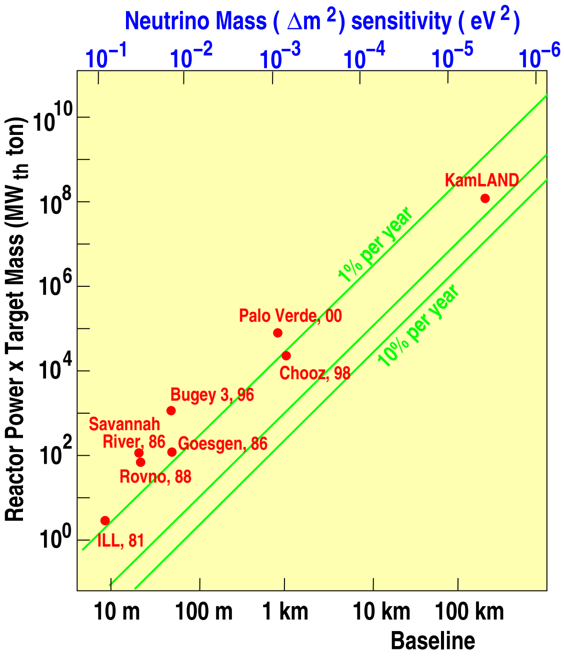

FIG. 3. Neutrino Δm^2 sensitivity as a function of total reactor power and detector fiducial mass for detection based on the inverse-β reaction discussed in the text. The baseline scales with the Δm^2 sensitivity sought according to Eq. (8). The fiducial-mass$\times$power necessary for the experiment grows with the square of the baseline. The past experiments are labelled by the name of the reactor complex used. The approximate year of the experiment is also indicated to show that the increased baseline and Δm^2 sensivity followed more or less the chronological order.

fact that the only known method of collimating neutrino beams employs the Lorentz boost of the parent particles from which decay the neutrinos are produced. For this reason low energy neutrinos are generally produced over large solid angles, while high energy ones may come in relatively narrow beams. Obviously a reactor emits $\bar{\nu}_e$ in a completely isotropic way, and this, together with the modest interaction cross-sections available at low energy, makes the specific signal rates rather low. At the same time, however, the low energy neutrinos provide us with a unique opportunity to probe the lowest regions of Δm^2 that are otherwise beyond the reach of accelerator-based searches. Some of these tradeoffs are well illustrated by Figure 3 where the Δm^2 sensitivity is shown, together with the necessary baseline, versus the reactor power and detector fiducial mass for different statistical accuracies.

Oscillation searches using reactors as sources are particularly important today since several of the indications for neutrino oscillations shown in Figure 1 point to regions of the parameter space at very small Δm^2 and nearly-full mixing. Hence two reactor-based experiments, Chooz and Palo Verde, were performed to investigate the phenomenon of atmospheric neutrinos as $\bar{\nu}_e \to \bar{\nu}_x$ oscillations. Such experiments, described in detail below, had baselines of about 1 km and fiducial masses of the order of 10 tons. For comparison, the much more complex accelerator-based Minos project between FNAL and the Soudan mine (Wojcicki 2001a) and analogous projects between CERN and Gran Sasso, Opera and Icarus (for a brief description, see e.g. Wojcicki 2001b), will access similar Δm^2 values with GeV-energy neutrinos and a baseline of the order of 1000 km. However, the 5400 ton Minos detector and its analog at Gran Sasso will be able to investigate also oscillation channels not including $\bar{\nu}_e$ and reach a mixing parameter sensitivity substantially better than 1%.

The reactor-based KamLAND experiment, with a baseline larger than 100 km, will offer the unique opportunity of testing, with man-made neutrinos, the large-mixing-angle MSW solution of the solar neutrinos puzzle. In this case the restriction to $\bar{\nu}_e \to \bar{\nu}_x$-oscillations does not limit the interest of the experiment (since solar neutrinos do certainly involve ν_e), while its Δm^2 sensitivity is well beyond what can be practically achieved by accelerators (for comparison similar Δm^2 sensitivity could be achieved in an accelerator-based experiment with baselines of order 10^5 km, larger than the diameter of the earth).

Of course, the relatively lower energy of neutrinos from reactors pushes the optimization of reactor-based experiments to concentrate on the reduction and rejection of backgrounds from natural radioactivity that is, on the other hand, hardly an issue in accelerator-based detectors. In this respect the correlated signature of the inverse-β process, the detection of the e^+ and neutron, plays a very important role.

While in the case of neutrinos produced by accelerators the experimenter has full control over the status of the beam, the flux of $\bar{\nu}_e$ cannot be changed at will in commercial power nuclear reactors. However, in practice, typical reactor optimization requires a refueling shutdown every 12 to 24 months. Such shutdowns usually last about a month, providing a convenient flux modulation that can be used to validate background subtraction methods. As explained in detail later, even in the case of KAMLAND that observes the neutrinos from about 70 reactor-cores, a substantial flux modulation is provided by the coincidence of scheduled refueling outages in the Spring and Fall periods, when electricity demand is lowest.

Finally, we remark here that the fully isotropic flux produced by nuclear reactors eliminates the problems related with beam pointing that are present in experiments using accelerators. While the pointing accuracy required in these experiments is well within the present technology, a fool-proof cross check of the beam-detector alignment is certainly not trivial to obtain.

In conclusion reactor-based and accelerator-based experiments offer complementary approaches to the quest for neutrino oscillations. It is likely that only the combined efforts on these two fronts, together with other studies such as the search for neutrino-less-double-β decay, will allow us to elucidate the problem of mixing in the lepton sector.

III. REACTOR NEUTRINO SPECTRUM AND FLUX DETERMINATION

Since reactor-based oscillation experiments are of the disappearance type, the accurate determination of the $\bar{\nu}_e$ spectrum and its absolute normalization are essential ingredients of the measurements. We note here that for oscillation parameters well within the experimental sensitivity the evidence for oscillations would manifest itself as a deficit of events accompanied by a distortion of the energy spectrum as shown by the example in Figure 4. However, as the true value of the oscillation parameters moves closer to the sensitivity boundary of the experiment, the spectral shape loses power and the accuracy of the measurements essentially relies on the total event count and, hence, the knowledge of the absolute reactor flux. This last scenario also corresponds to the more usual case in which no oscillations are observed and an upper-limit is set, as well as to the case of large Δm^2 where the spectrum distortions are washed out.

While in this section we will concern ourselves mainly with a-priori reactor $\bar{\nu}_e$ yield determinations, multiple-baseline measurements are possible and have been performed in the past at the Goesgen (Zacek *et al.* 1986) and Bugey (Achkar *et al.* 1995, 1996) reactors. Indeed such measurements helped gaining confidence in the reactor yield estimates, and, although were not the main goal of CHOOZ and PALO VERDE, have been recently proposed (Mikaelyan 2000) for a more accurate determination of the mixing angle θ_{13} for the atmospheric neutrino region. CHOOZ could take advantage of the ≈ 115 m distance between the reactors for deriving weaker exclusion limits, that were however less affected by systematics.

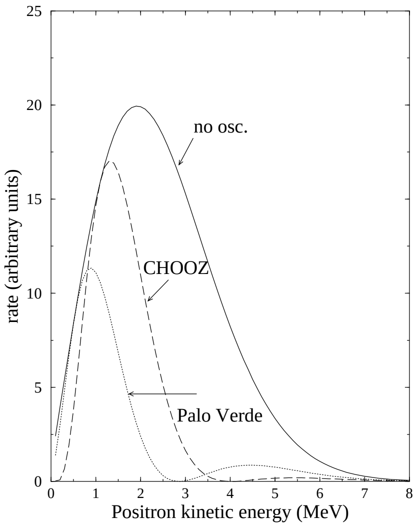

FIG. 4. Expected positron energy spectra for no oscillations (full line) and oscillations with parameters $\Delta m^2 = 7.2 \times 10^{-3}$ eV^2 and $\sin^2 2\theta = 1$ at the CHOOZ ($L \simeq 1$ km) (dashed line) and PALO VERDE ($L \simeq 0.8$ km) (dotted line) experiments. Adapted from Harrison, Perkins and Scott (1996).

A. Anti-neutrino production

The determination of the $\bar{\nu}_e$ yield proceeds, schematically, in three steps. First, the thermal power of each reactor core is measured, accurately and essentially continuously. Based on such measurements, and starting from the initial fuel composition, the burn-up state can be computed as function of time. Small corrections due to other reactor parameters that modify the criticality of the core are also introduced at this time. Reactor simulation codes are often used at this stage and produce an accurate instantaneous fission rate for each of the relevant isotopes through the fuel cycle. In the second step the neutrino spectrum is derived from the fission rate. Finally, as the last step, the neutrino spectrum emitted by the reactors must be converted into an estimate of the experimental observable, the positron spectrum in the detector. Each of these steps will be explained in a separate subsection.

Typical modern commercial Light Water Reactors (LWR) have thermal powers of the order of 3 GW_{th}. This figure applies to both Pressurized Water Reactors (PWR) and to the less common Boiling Water Reactor (BWR) designs. In both cases the fuel is enriched to 2-5% in ^{235}U. Since on average each fission produces $\sim$ 200 MeV and $\sim 6\ \bar{\nu}_e$ we conclude that the typical yield is $\sim 6 \times 10^{20}\ \bar{\nu}_e$ core^{-1} s^{-1} (of course part of this flux will be below the detection threshold, see Figure 2).

It is easy to understand why $\sim 6\ \bar{\nu}_e$ are produced per fission. Take, as an example, the most common ^{235}U fission, which produces two unequal fragments, and typically two new neutrons that sustain the chain reaction,

$$^{235}U + n \rightarrow X_1 + X_2 + 2n \ . \tag{12}$$

The mass distribution of the fragments (so-called fission yields) is shown in Fig. 5. The lighter fragments have, on average, $A \simeq 94$ and the heavier ones $A \simeq 140$. The stable nucleus with $A = 94$ is $_{40}$Zr^{94} and the stable $A = 140$ nucleus is $_{58}$Ce^{140}. These two nuclei have together 98 protons and 136 neutrons, while the initial fragments, as seen from the equation above, have 92 protons and 142 neutrons. To reach stability, therefore, on average 6 neutrons bound in the fragments have to β decay, emitting the required 6 $\bar{\nu}_e$.

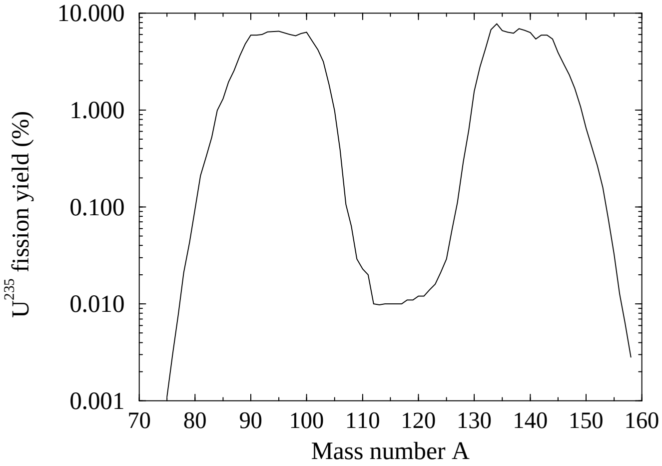

FIG. 5. Yields (in %) for ^{235}U thermal neutron fission (normalized to 2 for the two fragments)

While the total number of $\bar{\nu}_e$ is easy to estimate, and can be accurately determined given the known fission yields, their energy spectrum, which is of primary interest for the oscillation searches discussed here, requires more care. In particular, the commonly used neutrino detection reaction, the inverse neutron β decay, has $\sim$1.8 MeV threshold. Only about 1.5 $\bar{\nu}_e$/fission (i.e. $\sim$ 25%) of the total are above that threshold and hence can be detected, hence the total of $\sim$6 $\bar{\nu}_e$ per fission is irrelevant.

The existence of the 1.8 MeV threshold in the detection process $\bar{\nu}_e + p \rightarrow n + e^+$ automatically insures that only $\bar{\nu}_e$ from large Q-value, and hence short half-life, β-decays are detected. Thus the observed $\bar{\nu}_e$ signal tracks closely in time the power excursions in the reactor. This is of some practical importance as large quantities of spent fuel are usually stored on-site by reactor operators. There is no need to track the inventory of spent fuel and to worry about the β-decays of the neutron-activated reactor materials which have typically a low Q-value and therefore long half-life products. In practice, after a few hours from reactor turn on/off, the detectable $\bar{\nu}_e$ flux can be considered saturated.

B. Fission-rates determination

The four isotopes whose fission is the source of virtually all the reactor power are ^{235}U, ^{238}U, ^{239}Pu, and ^{241}Pu. The fission rates deriving from their evolution during a typical fuel cycle in one of the Palo Verde reactors is shown in Figure 6 as calculated by a core simulation program (Miller 2000). For comparison we also show the evolution of ^{240}Pu and ^{242}Pu that give the next to leading contributions. The contribution of these isotopes is of order 0.1% or less and will not be considered further.

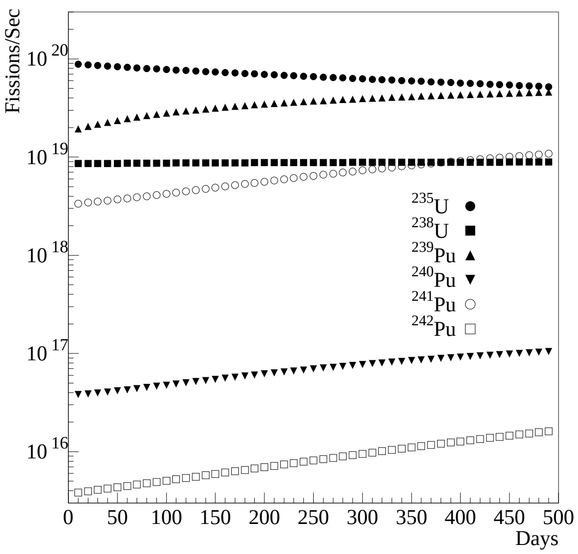

FIG. 6. Time evolution of fission rates for each of the six most important isotopes in one of the Palo Verde reactor cores. The horizontal scale covers a full fuel cycle, at the end of which about 1/3 of the core is replaced with fresh fuel. Only the four most important isotopes are normally used to predict $\bar{\nu}_e$ yields.

Each isotope produces a unique neutrino spectrum through the decay of its fission fragments and their daughters, so plutonium breeding results in a small but noticeable change in the emitted neutrino spectrum.

Two types of uncertainties can be attributed to the isotope compositions described in Figure 6: errors deriving from uncertainties in the initial fuel composition and in the measurement of the plant parameters that are used as input to the simulation, and errors due to imperfect core and neutronics modeling by the simulation program itself. The errors intrinsic to the simulation are known to contribute by substantially less than 1% to the neutrino yield from tests in which fuel is sampled and analyzed for isotopic composition at the end of a fuel cycle.

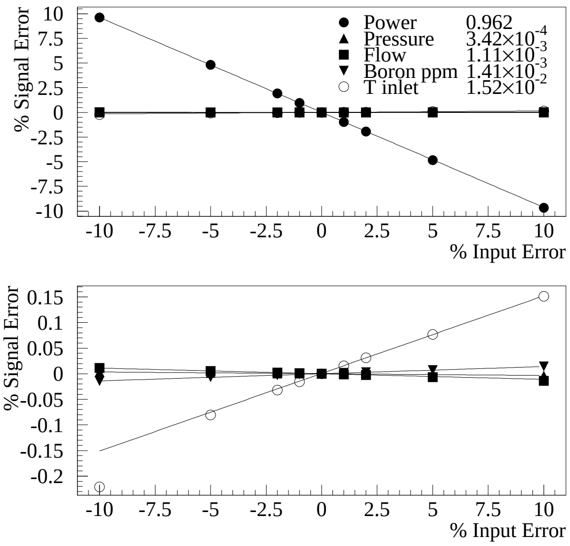

FIG. 7. Correlation between $\bar{\nu}_e$ yield and the five most important inputs to the core simulation for a PWR. The numbers in the key are the slopes of the fitted lines. Note that a variation of even 10% in any of the parameters, but power, has little effect on the output of the simulation.

The correlation between the $\bar{\nu}_e$ yield and the plant parameters used as input to the simulation is shown in Figure 7. Apart from the obvious correlation with the thermal power, other parameters enter the simulation because they affect the criticality by altering the neutron transport in the core (generally by the water density and boron absorber concentration). We see that for the parameter with largest correlation besides power, the water temperature in the cold legs, an error of 10% produce an uncertainty of only 0.15% in the $\bar{\nu}_e$ yield. Of course the inlet temperature is known to much better that 10%.

Economic and safety reasons provide plant operators with an incentive to accurately measure the thermal power of the reactors. Indeed, usually more than one method is used and the results are compared to understand the size of the uncertainties. Calorimetric methods (simultaneous measurement of temperature and flow-rate of the water outlet in the secondary cooling loop) give the smallest error ($\sim$ 0.6 - 0.7% at CHOOZ and PALO VERDE) and are used as primary power estimate.

C. From fission rates to the $\bar{\nu}_e$ spectra

The instantaneous fission rates of the four isotopes ^{235}U, ^{238}U, ^{239}Pu, and ^{241}Pu found above are then used as an input for the evaluation of the $\bar{\nu}_e$ spectrum. For all but ^{238}U careful measurements of the β spectrum from fission by thermal neutrons were performed (Schreckenbach *et al.* 1985, Hahn *et al.* 1989). These are converted to neutrino spectra as explained below. However, Refs. (Schreckenbach *et al.* 1985, Hahn *et al.* 1989) do not include ^{238}U that undergoes only fast neutron fission and hence was not accessible to such measurements.

There are, at present, several methods available to evaluate the $\bar{\nu}_e$ spectrum. For the $\bar{\nu}_e$ associated with ^{235}U, ^{239}Pu, and ^{241}Pu, which undergo thermal neutron fission, it is customary to use a hybrid method, based on the conversion of the measured electron spectra associated with the thermal neutron induced fission, into the $\bar{\nu}_e$ spectra. Clearly, the electron and $\bar{\nu}_e$ originate from the same β decay and share the available endpoint energy. For a single branch the conversion is therefore trivial. However, in general there are many branches, and many nuclei with different charges. For electron and antineutrino energies well above the electron mass the two spectra are quite similar (Schreckenbach *et al.* 1985)

$$\frac{\mathrm{d}N}{\mathrm{d}E_e} \simeq \frac{\mathrm{d}N}{\mathrm{d}E_{\bar{\nu}_e}} , \tag{13}$$

where $E_e = \sqrt{p_e^2 + m_e^2}$ is the full electron energy, and the proportionality constant deviates from unity by at most 5%. Naturally, one would like to convert the spectra more accurately.

Formally, the conversion can be performed exactly as follows. Let $n(E, Z)$, assumed to be a continuous function, describe the distribution of endpoints E and nuclear charges Z. The electron spectrum is then

$$Y(E_e) = \int_{E_e}^{\infty} \mathrm{d}E n(E,Z) k(E,Z) p_e E_e (E - E_e)^2 F(E_e, Z), \tag{14}$$

where $k(E, Z)$ is the spectrum normalization constant, p_e is the electron momentum, and $F(E_e, Z)$ is the Fermi function describing the Coulomb effect on the emitted electron. Provided that the electron spectrum $Y(E_e)$ is measured, the endpoint distribution can be determined,

$$n(E, Z) = -\frac{1}{2k(E,Z)} \frac{\mathrm{d}^3}{\mathrm{d}E^3} \left(\frac{Y(E)}{pEF(E,Z)} \right) . \tag{15}$$

Once the distribution $n(E, Z)$ is known, the $\bar{\nu}_e$ spectrum is readily calculated by the integral analogous to the Eq. (14). In (Davis *et al.* 1979, Vogel *et al.* 1981) it was shown that such conversion procedure depends only very weakly on the value of Z. In practice, an empirical relation $\bar{Z}(E)$ between the average $\bar{Z}$ and the electron energy has been used (Schreckenbach *et al.* 1985) ($\bar{Z} = 49.5 - 0.7E - 0.09E^2$ with E in MeV).

When using the measured electron spectra the above expressions, involving third derivatives, are obviously impractical. Instead, the integral in Eq. (14) is replaced by a finite sum of 30 hypothetical beta decay branches with branching ratios b_i and equidistant endpoints E_0^i,

$$Y(E_e) = \sum_i b_i k(E_0^i, \bar{Z}) \delta(E_e, E_0^i) p_e E_e (E_0^i - E_e)^2 F(E_e, \bar{Z}), \tag{16}$$

where $\delta(E_e, E_0^i)$ describes the small outer radiative corrections. One can now begin with the largest value of E_0^i (only one branch) and determine the corresponding branching ratio b_i using the electrons of energies between that E_0^i and the next smaller one, and continue in this fashion step by step until the smallest E_0^i is reached. Possible variations in the number and distribution of the endpoints E_0^i affects the resulting $\bar{\nu}_e$ spectrum not more than at 1% level (see Schreckenbach *et al.* 1985). Having determined the set b_i, E_0^i it is trivial to obtain

$$\begin{aligned} Y(E_{\bar{\nu}_e}) = \sum_i b_i k(E_0^i, \bar{Z}) E_{\bar{\nu}_e}^2 (E_0 - E_{\bar{\nu}_e}) \\ \times [(E_0 - E_{\bar{\nu}_e})^2 - m_e^2]^{1/2} F(E_0 - E_{\bar{\nu}_e}, \bar{Z}) \ , \end{aligned} \tag{17}$$

where the irrelevant radiative corrections were omitted. This is the procedure used in deriving the neutrino spectra associated with fission of ^{235}U, ^{239}Pu, and ^{241}Pu which account for about 90% of the reactor $\bar{\nu}_e$.

The $\bar{\nu}_e$ spectra in Refs. (Schreckenbach *et al.* 1985, Hahn *et al.* 1989, Davis *et al.* 1979, Vogel *et al.* 1981, Klapdor and Metzinger 1982a, 1982b) are given as tables. A somewhat less accurate, but easier to implement, analytical approximation is given in Vogel and Engel (1989). (The fit error to the total rate is about 1.2% for ^{235}U and only about 0.3% for ^{239}Pu and ^{241}Pu (Miller 2000).)

For the $\bar{\nu}_e$ associated with the ^{238}U fission one has to use the straightforward summation of the spectra of the $\bar{\nu}_e$ from all individual β^- decays. Thus

$$\frac{\mathrm{d}N}{\mathrm{d}E_{\bar{\nu}}} = \sum_n Y_n(Z, A, t) \sum_i b_{n,i}(E_0^i) P_{\bar{\nu}}(E_{\bar{\nu}}, E_0^i, Z) \ , \tag{18}$$

where $Y_n(Z, A, t)$ is the number of β decays per unit time of the fragment Z, A after the fissioning material has been exposed to neutrons for a time t and the label n characterizes each fragment. For t larger than the β decay lifetime of the fragment Z, A the quantity Y_n converges toward the cumulative fission yield and becomes independent of t. Naturally, each fission fuel is characterized by a different set of yields Y_n.

The quantities $b_{n,i}(E_0^i)$ in Eq. (18) are the branching ratios for the ith branch with the maximal electron energy (endpoint energy) E_0^i. The branching ratios are normalized to unity.

Finally, the function $P_{\bar{\nu}}(E_{\bar{\nu}}, E_0^i, Z)$ is the normalized spectrum shape. It is usually assumed, here and in the conversion method explained above, that all relevant β decays have the allowed shape,

$$\begin{aligned} P_{\bar{\nu}}(E_{\bar{\nu}}, E_0, Z) = k(E_0, Z) E_{\bar{\nu}}^2 (E_0 - E_{\bar{\nu}}) \\ \times [(E_0 - E_{\bar{\nu}})^2 - m_e^2]^{1/2} F(E_0 - E_{\bar{\nu}}, Z). \end{aligned} \tag{19}$$

To use Eq. (19) is a very good approximation in practice and causes a totally negligible error.

The weakness of this method is the incomplete information on the endpoint distribution and branching ratios of some fission fragments, in particular those with very short lifetimes and high decay energies. These 'unknown' decays contribute as much as 25% of the $\bar{\nu}_e$ at energies above 4 MeV. In practice, nuclear models are used to supplement the missing data. Examples of calculations based on this method are (Davis *et al.* 1979, Vogel *et al.* 1981, Klapdor and Metzinger 1982a, 1982b, Tengblad *et al.* 1989). An example of an extension to lower $\bar{\nu}_e$ energies, where the neutron activation of the reactor materials plays a role, is given by Kopeikin, Mikaelyan, and Sinev (1997).

While the summation method played an important role in the early oscillation searches, at present it is needed only for the description of the $\bar{\nu}_e$ from ^{238}U fission as pointed out above. That component contributes only about 11% to the neutrino signal. We show below that the error associated with the summation method is less than 10% and hence it contributes less than 1% to the overall uncertainty.

The ultimate check of the accuracy of the prediction outlined above consists in comparing the results in terms of $\bar{\nu}_e$ energy spectrum with the measurements performed in short baseline reactor oscillation experiments.

D. From $\bar{\nu}_e$ to positrons

Since in all reactor experiments one measures the positron spectra, and not directly the $\bar{\nu}_e$ spectra, one has to understand quantitatively how these are related. In other words, one has to know the cross section of the 'detector' reaction $\bar{\nu}_e + p \to e^+ + n$.

The total cross section for this reaction, neglecting terms of order E_ν / M, is given by the standard formula

$$\sigma_{tot}^{(0)} = \sigma_0 \ (f^2 + 3g^2) \ E_e^{(0)} p_e^{(0)}$$

$$= 0.0952 \left(\frac{E_e^{(0)} p_e^{(0)}}{1 \text{ MeV}^2} \right) \times 10^{-42} \text{ cm}^2 , \quad (20)$$

where $E_e^{(0)} = E_\nu - (M_n - M_p)$ is the positron energy when the (small) neutron recoil is neglected, and $p_e^{(0)}$ is the corresponding momentum. The vector and axial-vector coupling constants are $f = 1, g = 1.26$ and

$$\sigma_0 = \frac{G_F^2 \cos^2 \theta_C}{\pi} (1 + \Delta_{inner}^R) , \quad (21)$$

where the energy independent inner radiative corrections are $\Delta_{inner}^R \simeq 0.024$.

The cross section can be expressed in terms of the neutron lifetime and the phase space factor $f_{p.s.}^R = 1.7152$ (Wilkinson 1982) as

$$\sigma_{tot}^{(0)} = \frac{2\pi^2/m_e^5}{f_{p.s.}^R \tau_n} E_e^{(0)} p_e^{(0)} . \quad (22)$$

In this way, the cross section is tied directly to the neutron lifetime, known to 0.2% (Groom *et al.* 2000), no knowledge of G_F, f/g or the Cabibbo angle θ_C is in fact needed.

The (small) energy-dependent outer radiative corrections to σ_{tot} are given in Vogel (1984) and Fayans (1985). The corrections to the cross section of order E_ν/M, which are not negligible even for the reactor energies, and the angular distribution of the positrons are described in Vogel and Beacom (1999). The exact threshold of the reaction is

$$E_\nu^{thr} = \frac{(M_n + m_e)^2 - M_p^2}{2M_p} = 1.806 \text{ MeV} \quad (23)$$

instead of just $M_n + m_e - M_p = 1.804$ MeV when the recoil is neglected.

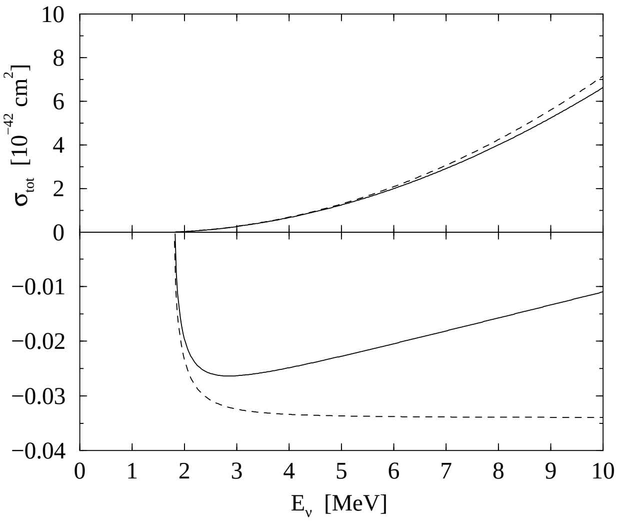

FIG. 8. Upper panel: total cross section for $\bar{\nu}_e + p \to e^+ + n$; bottom panel: $\langle \cos \theta \rangle$; as a function of the antineutrino energy. The solid line is the $\mathcal{O}(1/M_n)$ result and the short-dashed line is the $\mathcal{O}(1)$ result, Eq. 20.

Using the results of Vogel and Beacom (1999) one can evaluate the total cross section as well as the quantity $\langle \cos \theta_e \rangle$ which characterizes the positron angular distribution essentially exactly. These quantities are shown in Figure 8. The high energy extension of the total and differential cross section has been discussed already in the classic paper by Llewellyn-Smith (1972). Near threshold, however, that treatment must be modified as shown in Vogel and Beacom (1999).

The positron angular distribution, characterized by $\langle \cos \theta_e \rangle$ is rarely accessible. It is of interest, however, to consider also the angular distribution of the recoil neutrons that are also detected. Since in the laboratory system the proton is at rest, the neutron is initially emitted at a forward angle restricted by

$$\cos(\theta_n)_{max} = \frac{\sqrt{2E_\nu \Delta - (\Delta^2 - m_e^2)}}{E_\nu} , \quad (24)$$

where $\Delta = M_n - M_p \sim 1.3$ MeV. The average $\langle \cos(\theta_n) \rangle$ is considerably closer to unity (Vogel and Beacom 1999).

It is often possible to localize the points where the positron was created and where the neutron was captured and even though the neutron undergoes many elastic scatterings before capture, its final position maintains some memory of its original direction. Simulations suggest that the typical displacement of the two vertices is $\langle x \rangle \sim 1.5$ cm in the organic scintillator. In fact, in previous reactor experiments (Zacek *et al.*, 1986, Achkar 1992, Zacek 1984, Achkar *et al.* 1995) the neutron displacement was clearly observed, in the Goesgen experiment in particular, at $\simeq 10\sigma$ level. The same effect was also observed at Palo Verde. Moreover, the single vessel Chooz experiment was able to measure the average neutron-positron separation and to base on it a determination of the $\bar{\nu}_e$ incoming direction with an uncertainty of $\simeq 8°$ (Apollonio *et al.* 2000).

Given a reliable simulation of the neutron transport, this asymmetry allows, albeit with large errors, a direct measurement of the detector background. In case of $\bar{\nu}_e$ detection from a future Supernova, this technique may provide, as shown by Apollonio *et al.* (2000), a crude but useful determination of the direction to the $\bar{\nu}_e$ source, i.e. of the star position.

E. Accuracy of the flux and spectrum predictions

Once the cross section and $\bar{\nu}_e$ spectra are known, the corresponding positron yield is easily evaluated. In reactor experiments, the neutron recoil is quite small (10-50 keV) and thus the positron energy is simply related to the incoming $\bar{\nu}_e$ energy,

$$E_\nu \simeq (E_e + \Delta)\left[1 + \frac{E_e}{M_p}\right] + \frac{\Delta^2 - m_e^2}{M_p} \ , \tag{25}$$

where, as before, $\Delta = M_n - M_p$ and we used $\cos\theta_e = 0$ as a good approximation of the average $\langle\cos\theta_e\rangle$. We note here that possible detector efficiency dependence on the positron energy requires special care.

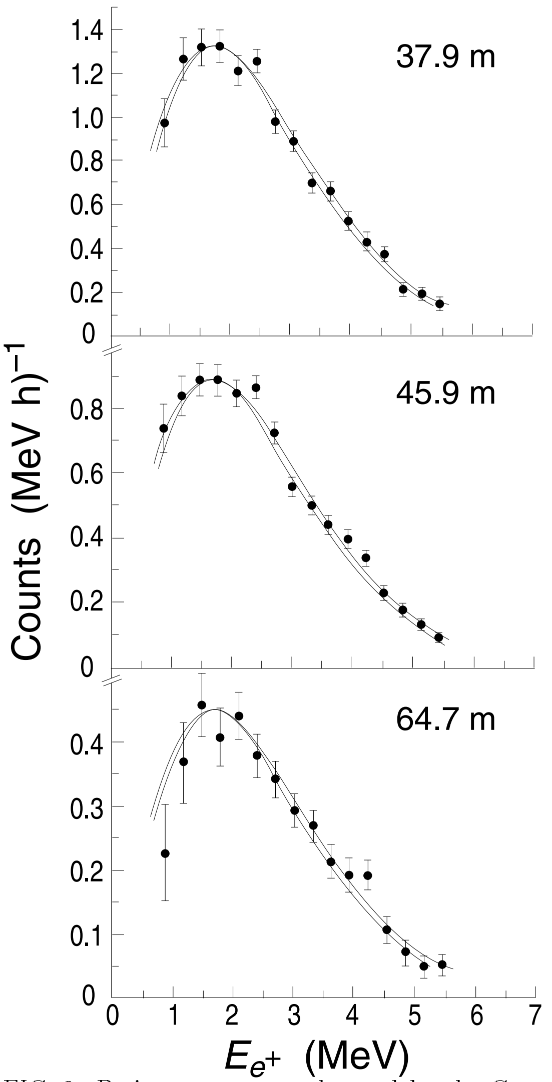

FIG. 9. Positron spectrum observed by the Goesgen experiment for three different baselines (Zacek 1984). The two continuous lines represent fits to the data and the predictions obtained, as described in the text, using the measurements (Schreckenbach *et al.* 1985, Hahn *et al.* 1989) for ^{235}U, ^{239}Pu, and ^{241}Pu and theoretical calculations for ^{238}U.

In order to check the accuracy of the prediction one has to compare the results, in terms of $\bar{\nu}_e$ energy spectrum and total flux normalization, with the measurements performed in short baseline reactor oscillation experiments. Since such experiments have not reported the observation of oscillations, we can assume that their measurements represent the direct determination of the reactor spectrum at production. There are four factors needed for the evaluation of the expected positron yield and spectrum: the distance to each core, the number of target protons, the cross section for $\bar{\nu}_e + p \to n + e^+$, and of course the quantity one wants to test, the $\bar{\nu}_e$ spectrum at the source.

The distance to the reactors is trivially obtained with negligible uncertainty. The number of protons in the target requires knowledge of the chemical composition and mass of both scintillator and possible other detector materials where $\bar{\nu}_e$ can be captured and recorded with finite efficiency. Typically errors smaller than 1% are achievable for this parameter. The cross section has been discussed at the previous subsection, and its uncertainty is also less than 1%. Finally, the $\bar{\nu}_e$ spectrum is the object of the test.

The $\bar{\nu}_e$ flux normalization alone was tested in Declais *et al.* (1994) where the total neutron yield was measured with high statistical accuracy, and found to be in agreement with the expectation based on the known neutron lifetime at the 3% level.

The validity of the tests performed at short distances from a reactor is reinforced by the fact that some of the experiments such as Goesgen (Zacek *et al.* 1986) or Bugey (Achkar *et al.* 1995, 1996) did measurements at different baselines observing no difference between the spectra. This is shown for Goesgen in Figure 9. Moreover, the relatively recent Bugey 3 measurements were performed at 15-40 m distance from the core and recorded very high statistics (some 1.5×10^5 $\bar{\nu}_e$ events).

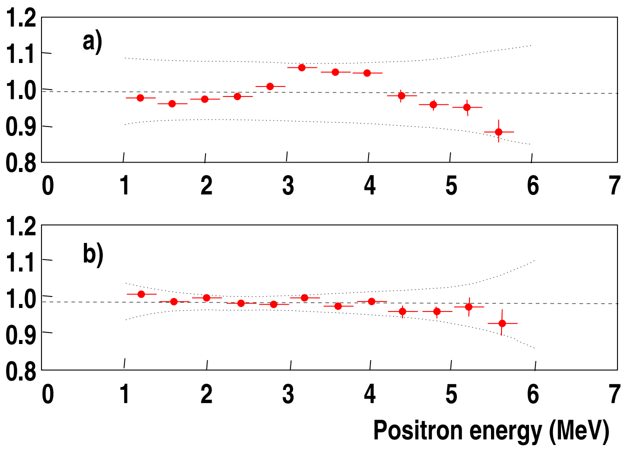

FIG. 10. Ratio between Bugey 3 measurements and different predictions. In a) the measurements are compared to the a-priori calculations of Klapdor and Metzinger (1982a, 1982b). In b) Bugey 3 data is compared to the prediction obtained using the β spectra measurements of Schreckenbach *et al.* (1985) and Hahn *et al.* (1989), and the calculation mentioned for ^{238}U. The dashed envelopes are estimates of the overall systematics. Adapted from Achkar *et al.* (1996).

The good agreement between Bugey 3 data and the non-oscillation predictions is demonstrated in Figure 10. In panel a) the prediction is generated purely from theory. Of more practical importance is panel b) where the prediction derives from β spectra (except for ^{238}U where theory is used). In this case a fit to a horizontal line gives a level of 0.99 with $\chi^2/d.o.f. = 9.2/11$. The final Bugey 3 result is quoted as having a 1.4% total uncertainty.

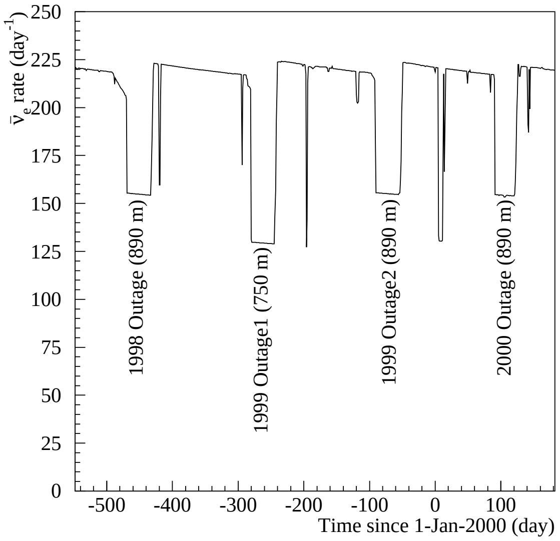

FIG. 11. Expected number of $\bar{\nu}_e$ interactions in the Palo Verde detector during the ~2 years of data-taking of the experiment. Note that one reactor is closer to the experiment while the other two are equidistant; this explains the different excursion for one of the refuelings. The steady decline in $\bar{\nu}_e$ interactions during the cycle is the effect of fuel burn-up.

For reference we give in Figure 11 the time evolution of the $\bar{\nu}_e$ interaction rate expected in the Palo Verde detector, calculated as described above from the plant data. This time evolution is typical of a plant with more than one reactor. Refueling outages (about 1 month long each) give different rate excursions due to the different distances between the reactors and the detector. Short accidental reactor trips are also visible along with the steady rate decline through the reactor cycle due to fuel burn-up.

In Fig. 12 the measured effect of the changing reactor fuel composition is shown. At the same time, the figure demonstrates how small that effect really is. We plot in Fig. 12 σ_f/E_f since the number of events n_ν at a given time and fuel composition is

$$n_\nu = \frac{1}{4\pi R^2}\frac{W_{th}}{\langle E_f\rangle}N_p\varepsilon\sigma_f \ , \tag{26}$$

where R is the distance, N_p the number of protons, ε is efficiency for the event detection, σ_f is the effective cross section per fission and $\langle E_f\rangle$ is the average energy per fission which are both sensitive to the burn-up.

In conclusion, the $\bar{\nu}_e$ spectra, and its absolute normalization, are known to about 2% accuracy. Obviously, the reactors as $\bar{\nu}_e$ sources are perfectly isotropic. The differences between various reactors, and the time changes due to the fuel burn-up are small, and well understood. They do not cause additional uncertainty. Thus, for the reactor neutrino oscillation searches at a few percent accuracy, no short distance 'monitor' detectors are needed. One can simply compare the measured positron spectra at the distance L to the expectation at the source ($L = 0$).

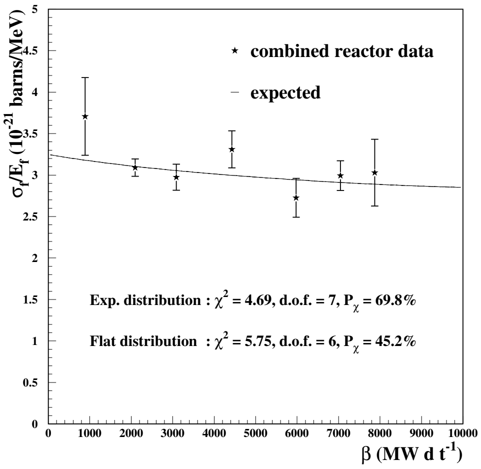

FIG. 12. The measured $\bar{\nu}_e$ event rate at Chooz, expressed as the cross section per fission divided by the energy per fission (see text for explanation), as a function of the reactor burn-up (in units of MW×days per ton), i.e., the accumulated reactor power per unit mass of fuel. The fits to the expected rate, which includes the reactor burn-up, and to the flat rate, where the burn-up is neglected, are also shown. Adapted from Nicolò (1999).

F. Other reactor neutrino experiments

We shall only briefly mention here other experiments with reactor $\bar{\nu}_e$ that are of importance as a potential source of information about neutrino intrinsic properties. Besides protons, two targets have been extensively studied: deuterons and electrons.

Reactor $\bar{\nu}_e$ can cause deuteron disintegration by two reaction channels; the charged current (CC)

$$\bar{\nu}_e + d \to e^+ + n + n \ , \tag{27}$$

with the threshold of 4.03 MeV ($M_n + m_e - M_p + B$), where B is the deuteron binding energy, and the neutral current (NC)

$$\bar{\nu}_e + d \rightarrow \bar{\nu}_e + p + n \ , \tag{28}$$

with lower threshold of $B = 2.23$ MeV. The cross sections of these reactions, $\sim 1.1 \times 10^{-44}$ cm^2/fission for the CC, and $\sim 3.1 \times 10^{-44}$ cm^2/fission for the NC (see e.g. Davis *et al.* (1979) and Vogel *et al.* (1981)) are more than an order of magnitude smaller than for the reaction on the proton target. (The cross section is expressed 'per fission' because the fission rate is the quantity more directly related to the reactor power than the $\bar{\nu}_e$ flux.)

The study of the $\bar{\nu}_e + d$ reactions was pioneered by Reines and collaborators (Pasierb *et al.* 1979, Reines *et al.* 1980), who observed the corresponding two or one neutron captures. From the point of view of neutrino oscillations, the ratio of the CC and NC rates is potentially useful, since the CC is flavor sensitive and NC is not (the same idea is being pursued in the case of solar neutrinos by the SNO collaboration). More recent experiments (Riley et al. 1999, Kozlov et al. 2000) show, as expected given the short distance from the reactor, no indication of oscillations.

The other reaction observed with the reactor $\bar{\nu}_e$ is the scattering on electrons

$$\bar{\nu}_e + e \rightarrow \bar{\nu}_e + e \ , \tag{29}$$

where the spectrum of the recoil electrons (originally assumed at rest in the laboratory since the electron momentum associated with the atomic binding is usually negligible) is observed. Obviously, the reaction signature, just the recoiling electron, is quite difficult to distinguish from background caused by radioactivity, making the observation of the $\bar{\nu}_e - e$ scattering very challenging.

The cross section for $\bar{\nu}_e - e$ scattering consists of the well understood weak interaction part, and a so far unobserved incoherent electromagnetic part:

$$\frac{\mathrm{d}\sigma}{\mathrm{d}T} = \frac{G_F^2 m_e}{2\pi}\left[(f+g)^2 + (f-g)^2 \times \left(1 - \frac{T}{E_\nu}\right)^2 + (g^2 - f^2)\frac{m_e T}{E_\nu^2}\right] + \frac{\pi\alpha^2\mu_\nu^2}{m_e^2}\frac{1 - T/E_\nu}{T} \ , \tag{30}$$

where T is the kinetic energy of the recoiling electron. The first part, weak scattering, represents the sum of coherent (interfering) contributions from charged and neutral currents, while the second part, proportional to α^2, can be described as due to a finite neutrino magnetic moment μ_ν. Only massive neutrinos can have magnetic moments, and hence the study of this reaction, and the possible determination of μ_ν^2, is of great interest.

Again, pioneering results were obtained by Reines and collaborators (Reines, Gurr and Sobel 1976). More recently, limits on μ_ν^2 with reactor neutrinos, albeit with a rather poor signal to noise ratio, were obtained by Derbin *et al.* (1993). At present a slightly more stringent direct limit of $\mu_\nu \leq 1.6 \times 10^{-10}\mu_{\mathrm{B}}$ comes not from the reactor neutrinos, but from the analysis of the shape of the Super-Kamiokande (Fukuda *et al.* 1999) solar neutrino data (Beacom and Vogel 1999). A new effort to improve the sensitivity to μ_ν^2 is currently underway (Amsler *et al.* 1997) at the Bugey reactor (MUNU experiment).

IV. EXPERIMENTS MOTIVATED BY THE ATMOSPHERIC NEUTRINO ANOMALY

Two experiments have been built with the specific purpose of testing the hypothesis that neutrino oscillations occur with the parameters found by the atmospheric neutrino measurements. Both experiment are now completed. All Chooz data are published in Apollonio *et al.* 1998, 1999, and Nicolò 1999. Data-taking at Palo Verde finished in the summer 2000 and the results are published in Boehm *et al.* 2000a, 2000b, 2001, and Miller 2000.

As it can be seen from Figure 3, in order to access $\Delta m^2 \approx 10^{-3}$ eV^2 with reactor neutrinos, a baseline of order 1 km and a mass in excess of a few tons are needed. Indeed, the backgrounds from cosmic radiation and natural radioactivity are a major consideration in the design of such large, low-energy detectors, and different backgrounds situations led the two groups to rather different designs.

The Chooz detector was built in a pre-existing underground cavity under a $\simeq$ 100 m rock overburden ($\simeq$ 300 m.w.e). This substantial cosmic radiation shielding allowed the use of a homogeneous detector where inverse-β events were tagged as a double (delayed) coincidence between the e^+ (prompt) signal and the n (delayed) one. Such simple event signature can be identified with large efficiency so that a 5 ton active mass was sufficient for the experiment. The Palo Verde detector, on the other hand, was located in an underground bunker excavated for the purpose. Economic considerations limited the overburden to 12 m ($\simeq$ 32 m.w.e.) sufficient only to eliminate the hadronic component of the cosmic radiation and reduce the muon flux by a factor of five. The rather large remaining muon flux produced a substantial quantity of secondary neutrons so that a segmented detector was needed to take full advantage of the triple coincidence given by the e^+ ionization and subsequent γ's from annihilation. This more elaborate topological signature reduced the detector efficiency and pushed the fiducial mass to 12 ton. Both detectors were built with materials selected for low radioactivity and included a passive γ and neutron shield and an active cosmic-ray veto counter.

While the 3-reactor plant of Palo Verde produces a larger power (11.6 GW$_{th}$) than the 2-reactor one at Chooz (8.5 GW$_{th}$), more important is the fact that, unlike in the case of Palo Verde which was a plant already running for a long time, the CHOOZ reactors were commissioned after the start of data taking of the experiment. This endowed the collaboration with the rather unique opportunity of observing the backgrounds at reactor-off for a substantial period and the slow ramp-up of power. On the other hand the need to cope with a much more stable operation, with the periodic $\sim 2/3$ refueling power excursions shown in Figure 11, motivated the PALO VERDE group to develop new methods for background subtraction that will be important for future experiments likely to run in similar steady-state situations.

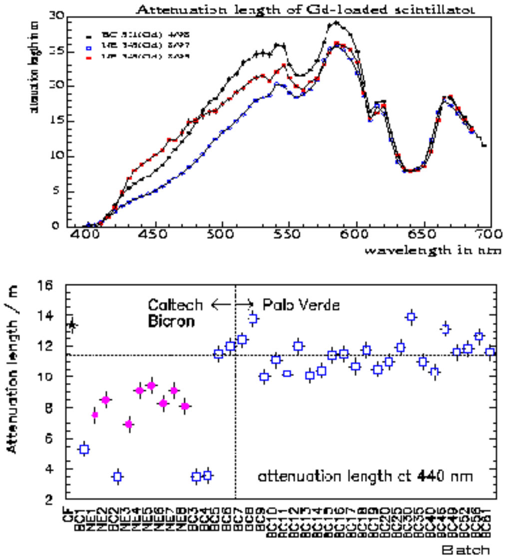

FIG. 13. Initial light attenuation length in PALO VERDE scintillator. Top: attenuation length as function of wavelength in three pre-production batches. Bottom: attenuation length at $\lambda = 440$ nm for the initial batches of scintillator. Production batches are to the right of the vertical dashed line, while on the left we show various test batches not used in the detector. The first point ("CF") refers to a standard (non Gd loaded) scintillator fluid. Typical production scintillator had an attenuation length better than 11 m.

Both detectors used liquid scintillator loaded with 0.1% natural gadolinium which has a high thermal neutron capture cross-section and releases a large amount of energy in the capture. In this way the neutron capture time is reduced to $\sim$27 μs from $\sim$170 μs for the unloaded scintillator, proportionally reducing the uncorrelated background. Furthermore, Gd de-excitation after the capture releases a 8 MeV γ cascade, whose summed energy gives a robust event tag well above natural radioactivity. In contrast, neutron capture on protons results only in a single 2.2 MeV γ. While the Gd loading offers obvious advantages in suppressing backgrounds, it is not easy to achieve in the stable and sufficiently transparent form needed for a large detector. Both groups invested substantial resources in scintillator development. In Figure 13 we show initial attenuation length data for the PALO VERDE scintillator that was a cocktail of 60% mineral oil, 36% pseudocumene (1,2,4 trimethylbenzene) and 4% alcohol (used to keep the Gd compound in solution), with PPO as primary fluor. This scintillator had a H:C ratio of $\simeq 2$ and a light yield of 56% of anthracene, with typical light attenuation length greater than 11 m at $\lambda = 440$ nm (Piepke *et al.* 1999).

The time stability of the same scintillator is shown in Figure 14 where the light attenuation curve for one cell and the *effective* attenuation length for all cells are presented as measured three times, at one year intervals. The 12% loss in the first year decreases to 3% in the second, possibly indicating a gradual stabilization.

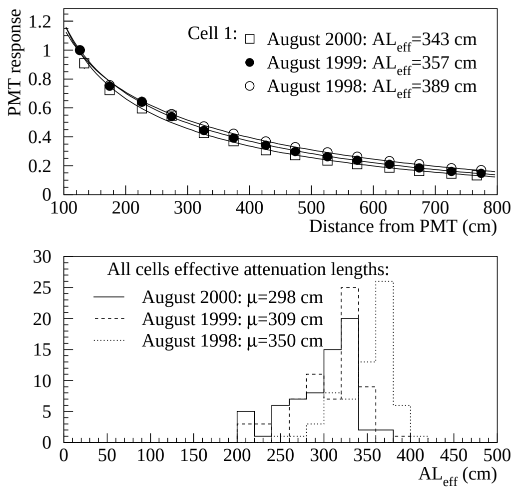

FIG. 14. Evolution of scintillation-light attenuation-length in PALO VERDE scintillator during the two years of life of the detector. Top: the attenuation curve for scintillation events at different locations along one of the 9 m-long cells. Bottom: *effective* attenuation values for all detector cells. Note that the shorter value of the effective attenuation length reflects the non-trivial optics of the cells.

The time variation of the attenuation length λ_{Gd} of the Gd-loaded scintillator at CHOOZ, regularly measured in the detector, is well fitted by the empirical function

$$\lambda_{Gd}(t) = \frac{\lambda_0}{1 + \alpha t} \tag{31}$$

which accounts for the observed exponential decrease of the signal with time. Results of the fit are shown in Figure 15.

The properties of the Gd-loaded and unloaded veto liquid scintillators developed for CHOOZ are presented in Table I.

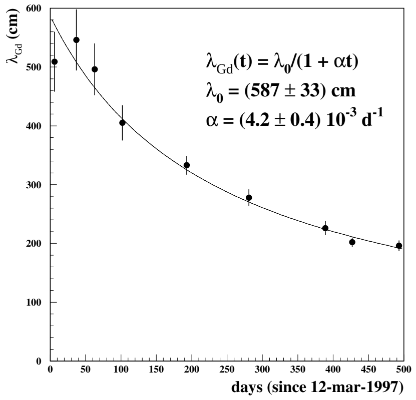

FIG. 15. Light attenuation length λ_{Gd} of the CHOOZ Gd-loaded scintillator versus time with best-fit function shown.

TABLE I. Main properties of the liquid scintillators used in the CHOOZ experiment.

	Gd-loaded	unloaded
Chem. cont.:		
basic	Norpar-15** (50% vol.)	Mineral oil (92.8% vol.)
aromatics, alcohols	IPB+hexanol (50% vol.)	IPB (7.2% vol.)
wavelength shifters	p-PTP+bis-MSB (1 g/l)	PPO + DPA (1.5 g/l)
Atomic mass composition:		
H	12.2%	13.3%
C	84.4%	85.5%
Gd	0.1%	
others	3.3%	1.2%
compatibility	acrylic, teflon	
density (20°)	0.846 g/l	0.854 g/l
Flash point	69°	110°
Scint. yield	5300 photons/MeV ($\simeq$ 35% of anthracene)	
Optical atten. length	4 m	10 m
Refr. index	1.472	1.476
Neutron capture time	30.5μs -	180μs
Thermal neutron capture path	$\sim$ 6 cm	$\sim$ 40 cm
Capture fraction on Gd	84.1%	

**Norpar-15 is the trademark of Exxon Mobil Corporation.

A. Chooz

The CHOOZ detector was built at the distances of 1115 m and 998 m from the two reactors of the new CHOOZ power plant of *Électricité de France* in the Ardenne region of France. The plant, shown in Figure 20, has a total thermal power of 8.5 GW_{th} and the two reactors reached full power in, respectively, May and August 1997. The experiment took data from April 1997 until July 1998, in the conditions specified in Table II.

The apparatus, schematically shown in Figure 16, consisted of a central volume of scintillator with a mass of 5 tons, where $\bar{\nu}_e$ were detected. This scintillator was contained in an acrylic vessel (region 1) that separated it from a 70 cm thick shielding layer of mineral oil (region 2). 192 eight-inch photomultipliers (PMT's) were mounted onto a steel vessel that, in-turn, isolated, mechanically and optically, the central detector from the outer veto counter. The central detector had a photocathode coverage of 15% and a light yield of $\sim$ 130 photoelectrons/MeV (p.e./MeV) (Baldini *et al.* 1996). The 90 ton veto scintillator was at least 80 cm thick and was readout with two rings of 24 eight-inch PMT's, the outer containment tank being painted with white reflective paint. An outer layer (75 cm thick) of low-activity sand provided primary shielding from the rock.

Laser flashers were installed to monitor the detector performance and radioactive sources could be inserted into the central region of the detector through special pipes. The detector energy response was calibrated daily with ^{60}Co, ^{252}Cf and AmBe γ- and n-sources in order to accurately track the aging of the scintillator, the detector efficiency and the energy calibration.

As an example we show in Figure 17 the results of a Cf calibration run with the source placed in the middle of the detector. Data is compared with a Monte Carlo simulation for the reconstruction of the x, y and z positions and total energy in the detector. Both the peaks for n-captures on p (2.2 MeV) and Gd (8 MeV) are clearly visible. The very good energy resolution ($\sigma(E)/E = 5.6$ % at 8 MeV) allows one to verify that the 8 MeV peak is in fact the superposition of a 7.77 MeV line with 77% weighting from capture on ^{157}Gd (energy shifted from

TABLE II. Summary of the CHOOZ data-taking conditions.

	Time (h)	$\int W_{th} dt$ (GWh_{th})
Total run	8761.7	
Live	8209.3	
Dead	552.4	
Reactor 1 ON only	2058.0	8295
Reactor 2 ON only	1187.8	4136
Both reactors ON	1543.1	8841
Both reactors OFF	3420.4	0

7.94 MeV because of scintillator saturation effects) and a 8.31 MeV line with 23% weighting from capture on ^{155}Gd (energy shifted from 8.54 MeV). The fit to these two Gaussians gives χ^2/d.o.f. = 67.6/55 while the fit to a single Gaussian is very poor with χ^2/d.o.f. = 875/58. The position resolution was found to be $\sigma_x = \sigma_y = \sigma_z =$ 17.5 cm.

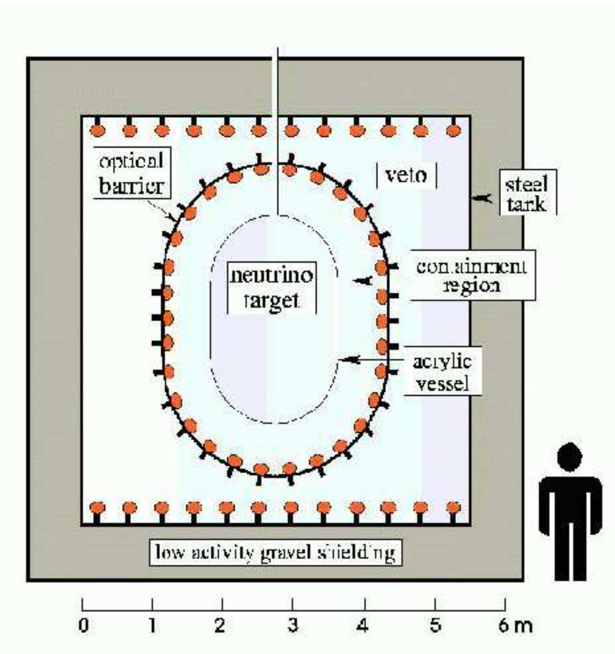

FIG. 16. Schematic drawing of the CHOOZ detector.

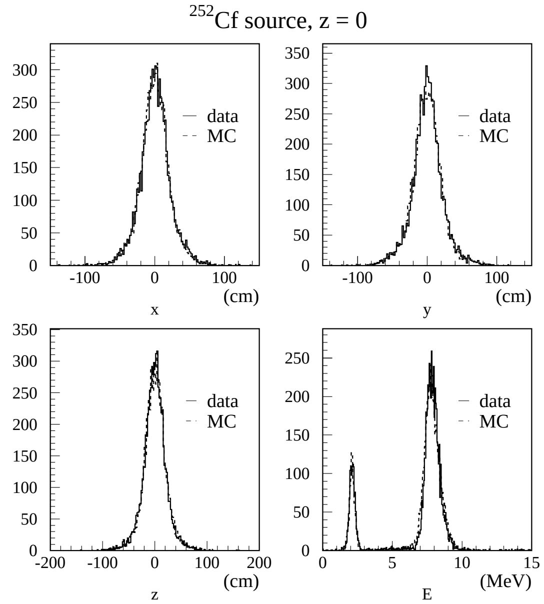

FIG. 17. Visible energy and position reconstructed for a calibration ^{252}Cf source placed inside the CHOOZ detector.

B. Palo Verde

The PALO VERDE experiment was built at the Palo Verde Nuclear Generating Station, the largest nuclear plant in the Americas, ∼ 80 km west of Phoenix, in the Arizona desert. The total thermal power from three identical pressurized water reactors is 11.6 GW$_{th}$. Two of the reactors were located 890 m from the detector, while the third was at 750 m. The shallow underground bunker housing the detector is shown in Figure 21 at the time of construction. In total 350.5 days of $\bar{\nu}_e$ data were collected at PALO VERDE in the period between October 1998 and July 2000, covering four scheduled refueling outages as indicated in Figure 11. Of these, 242.2 days were at full power, while 21.8 days (86.5 days) had the reactor at 750 m (890 m) off. Such data was complemented by frequent calibration runs.

The fiducial mass, segmented for active background rejection, consisted of 66 acrylic tanks filled with 0.1% Gd-loaded scintillator and arranged as shown in Figure 18. Each cell was 9 m long, with a 12.7 × 25.4 cm^2 cross section, and it was viewed by two 5-inch photomultiplier tubes, one at each end. A $\bar{\nu}_e$ is identified by space- and time-correlated e^+ and n signals. Positrons deposit their energy in a scintillator cell and annihilate, yielding two 511 keV γ's that, in general, will be detected in different cells, giving a triple coincidence. Neutrons thermalize and are captured in Gd, giving a γ-ray shower of 8 MeV total energy also detected in more than one cell. The central detector was surrounded by a 1 m-thick water shield to moderate background neutrons produced by muons outside the detector and to absorb γ's from the laboratory walls. Outside of the water tanks were 32 large liquid scintillator counters and two end-caps to veto cosmic muons. The rate of cosmic muons was approximately 2 kHz. The pattern of muons traveling through veto counters and their timing relative to the central detector hits were recorded for subsequent off-line analysis. The central detector was equipped with a system of tubes that allowed the insertion of calibration sources in the small spaces between cells. In addition, a set of blue LEDs and optical fibers was used to produce flashes of light inside each of the cells. In order to reduce natural radioactivity, all building materials for the detector were carefully selected, including the aggregate (marble) used in the concrete of the underground laboratory.

Both the positron and the neutron were triggered by a triple coincidence requiring at least one cell above a "high" threshold set at ∼600 keV (positron ionization or neutron capture cascade), and two cells above a "low" threshold set at ∼40 keV (Compton scattering from annihilation photons or neutron capture cascade tails). The triple coincidences were required to be within 3×5 matrices of cells anywhere in the detector as recognized by a custom-made trigger processor (Gratta *et al.* 1997).

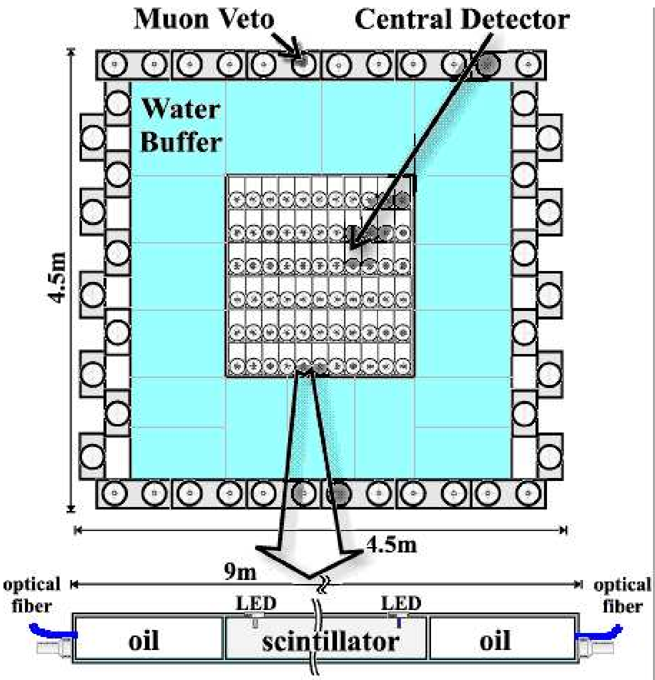

FIG. 18. Schematic view of the PALO VERDE neutrino detector.

The efficiency calibration was based upon a primary measurement performed a few times per year with a calibrated ^{22}Na e^+ source and an Am-Be neutron source. The ^{22}Na source mimicked the effects of the positron from the $\bar{\nu}_e$ interaction by providing annihilation radiation and a 1.275 MeV photon which simulated the e^+ ionization in the scintillator. The source was placed at 18 positions in the detector deemed to be representative of different conditions. The results of this procedure were then rescaled to the e^+ case using a Monte Carlo simulation. The neutron detection efficiency was measured by scanning the detector with the Am-Be source where the 4.4 MeV γ associated with the neutron emission was tagged with a miniaturized NaI(Tl) counter. Other calibrations, used to measure the detector energy response, were performed using the Compton edges from ^{137}Cs, ^{65}Zn and ^{228}Th sources. The same Th source was also used more frequently to track the scintillator transparency, as already shown in Figure 14. Weekly runs of the fiber-optic and LED flasher systems were used, respectively, to monitor the gain and linearity of photomultipliers and the timing/position relationship along the cells.

Since the energy deposition of the 511 keV γ's in one cell has a sharp falling spectrum (Compton scattering) it was vital to have the lowest possible "low" thresholds in the trigger and to understand the behavior of such thresholds with great accuracy. This second task was complicated by the fact that the trigger used voltage amplitudes, while only charge from integrating ADCs was available off-line. For this reason the detector simulation included a detailed description of the signal development in time. This code correctly described the shape of pulses taking into account scintillator light yield, attenuation length and de-excitation time; photomultiplier rise- and fall-time and gain; and event position along a cell. The simulation of the detector response to the ^{22}Na source is shown in Figure 19 and correctly describes the 40 keV (600 keV) threshold position to within 1.4 keV (2.6 keV), resulting in uncertainties on the positron and neutron efficiencies of 4% and, respectively, 3%.

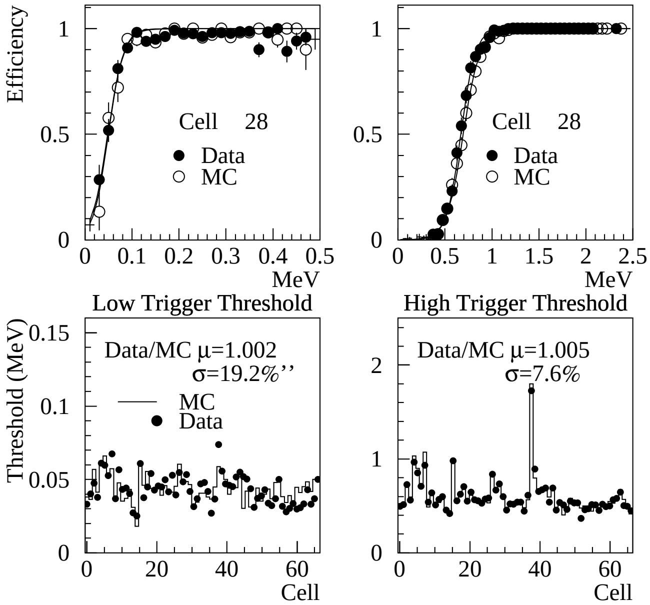

FIG. 19. A comparison of the trigger thresholds at PALO VERDE from data and Monte Carlo. The data were taken with a ^{22}Na source at the center of each cell. The top portion shows the efficiency of the trigger thresholds (low and high) for a typical cell as a function of energy deposited; the bottom shows the energy at 50% efficiency for low and high thresholds in all 66 cells.

C. Backgrounds

There are generally two types of background affecting long baseline reactor experiments where the signal is based on the correlated e^+, n signature: uncorrelated hits from cosmic-rays and natural radioactivity and correlated ones from cosmic-μ-induced neutrons. The first type can be measured by studying the time difference between positron-like and neutron-like parts of an event. More insidious are cosmic-μ-induced neutrons that present the same time and space correlation between prompt and delayed parts of the event as in $\bar{\nu}_e$. Such events are schematically shown in the PALO VERDE detector, in Figure 22. Neutrons are produced by cosmic-μ spallation and capture on the materials outside the veto counter. Both production mechanisms can result in either neutron thermalization and capture, where the thermalization process fakes the prompt triple coincidence, or secondary neutrons production, where one of the captures fakes the prompt triple coincidence. Conceptually the same situation holds for CHOOZ (and KAMLAND, as it will be discussed later), although differences in overburden and the simpler scheme of coincidence, numerically change the relative importance of different backgrounds. It is useful to point out that direct neutrons from the reactors have a totally negligible effect at the distances discussed here.

Both experiments pre-select $\bar{\nu}_e$ candidates by requiring an appropriate topology (in space and time) for the prompt and delayed parts of each event and their relative position. Such cuts insure that the spatial and temporal extents of the events are compatible with the $\bar{\nu}_e$ hypothesis and that events are well contained and measured in the detector. A general classification in terms of signal and different backgrounds can be conveniently done by studying the correlation between prompt and delayed energy in CHOOZ for such pre-selected sample, as shown in Figure 23. The region marked "B" in the Figure contains cosmic-ray muons stopping in the detector after entering undetected by the veto counter. Both prompt energy (muon ionization) and delayed energy (Michel electron) are large. Indeed events in region "B" show a fast time correlation between prompt and delayed part, consistent with the muon lifetime. Region "C" is populated by the muon-spallation events discussed above: large prompt energy deposit from proton recoils in neutron thermalization is accompanied by a fix 8 MeV energy deposit characteristic of neutron capture. Regions "A" and "D" are populated by random coincidences of natural radioactivity hits, sometimes including a high-energy proton recoil from neutron scattering in the delayed part (region "A"). Neutrino candidates populate the region framed by the darker line, as it can be seen by comparison between the scatter plots with reactors ON and OFF.

The time elapsed between the prompt and delayed parts of the events is shown in Figure 24 for the PALO VERDE data. We note that the process of n-capture in the segmented detector requires the sum of two exponentials to fit properly. This is due to the fact that a fraction of the neutrons stop, after thermalization, in passive materials (mainly acrylic for PALO VERDE) where there is no Gd and the capture is a slower process. While the Monte Carlo gives a good fit with two exponentials, for data a third exponential, with longer time constant, is needed in the fit. Such exponential accounts for events initiated by uncorrelated background, having the delayed part triggered by cosmic rays, crossing the detector with a 2 kHz rate. Timing cuts are applied by both experiments to insure that events are consistent with a neutron capture. In addition events are rejected for a period of time following tracks detected in the veto counters. This last cut is particularly important at PALO VERDE where the cosmic-ray rate is high.

The availability for CHOOZ of data at zero power and with the reactors ramping up provides an independent way to check the magnitude of signal and background. The fitting procedure proceeds as follows. For each run the predicted number of neutrino candidates resulting from the sum of a signal term, linearly depending on the reactor effective power W^* , and the background, assumed to be constant and independent of power ††; so,

$$\overline{N}_i = (B + W_i^* X)\Delta t_i, \tag{32}$$

where the index i labels the run number, Δt_i is the corresponding live time, B is the background rate and X is the positron yield per unit power averaged over the two reactors.

The results are listed in Table III, for three data taking periods corresponding to threshold readjustments. The data are also shown in a compact form in Figure 25.

A simple subtraction of the e^+ spectra with reactor ON and OFF gives for CHOOZ the spectrum shown in Figure 26. The comparison of the observed distribution with the expected one for no-oscillations already shows very good agreement.

TABLE III. Summary of the likelihood fit parameters for the three data taking periods at CHOOZ .

period	1	2	3
starting date	97/4/7	97/7/30	98/1/12
runs	579 $\rightarrow$ 1074	1082 $\rightarrow$ 1775	1778 $\rightarrow$ 2567
live time (h)	1831.3	2938.8	3268.4
reactor-off time (h)	38.9	539.5	2737.2
$\int W dt$ (GWh)	7798	10636	2838
B (counts/d)	1.25 ± 0.6	1.22 ± 0.21	2.2 ± 0.14
X (counts/d GW)	2.60 ± 0.17	2.60 ± 0.09	2.51 ± 0.17
χ^2/dof	136/117	135/154	168/184
N_ν (counts/d) (@full power)	24.8 ± 1.6	24.8 ± 0.9	24.0 ± 1.6

††The "effective" power W^* is a fictitious thermal power corresponding to both reactors located at the reactor 1 site, and thus providing 9.55 GW at full operating conditions and at starting of reactor operation.

FIG. 20. Aerial view of the CHOOZ power plant. The detector is located in a tunnel under the hills on the bottom right of the photograph.

FIG. 21. The PALO VERDE underground laboratory at the time of construction (Fall 1996).

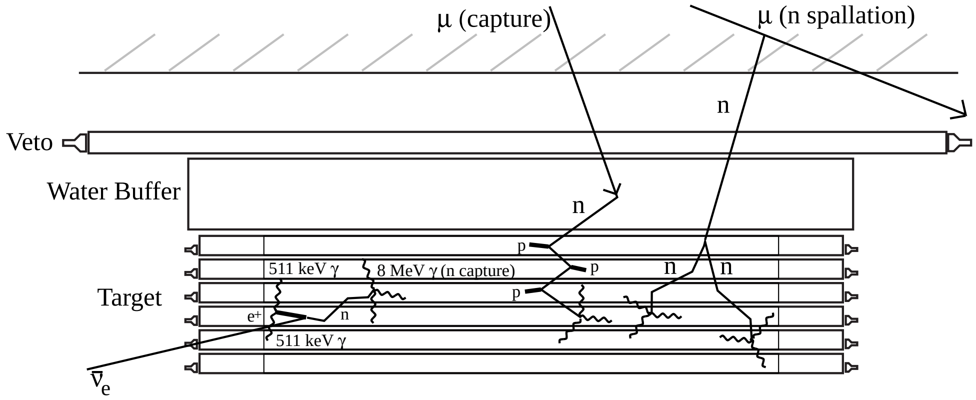

FIG. 22. Schematic view of two types of cosmic-μ-induced backgrounds and a signal event (far left) in the Palo Verde detector. Neutrons are produced by cosmic-μ spallation (right) and capture (left) on the materials outside the veto counter. Both can result in either neutron thermalization and capture (left), where the thermalization process fakes the prompt triple coincidence, or secondary neutrons production (right), where one of the captures fakes the prompt triple coincidence.

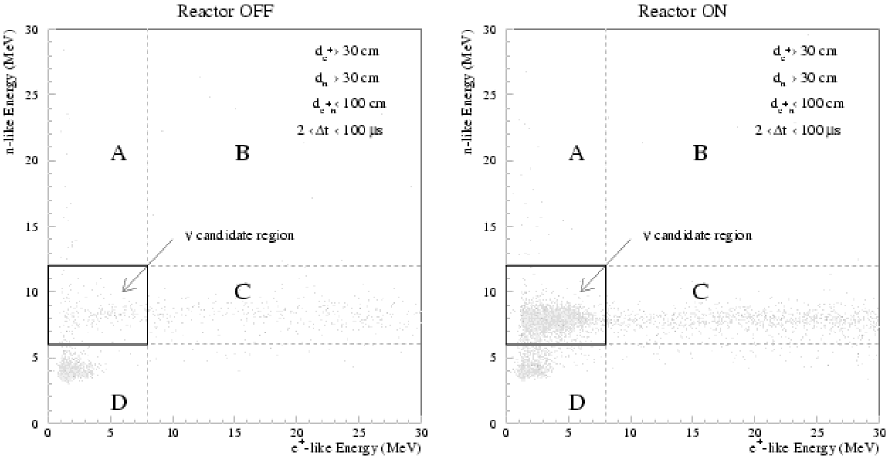

FIG. 23. Delayed energy vs. prompt energy in pre-selected Chooz events. The selection cuts are listed in the figure. On the left it is shown the case of reactors OFF, while on the right is the case of reactors ON. A description of the event-types in the different regions of the plot is given in the text.

TABLE IV. Summary of results from the Palo Verde experiment (Boehm *et al.* 2001). Uncertainties are statistical only. N, N' and $(1-\epsilon_1)B_{\rm pn}$ are measured rates, while Background and R_ν are efficiency corrected (assuming that the background events are measured with the same efficiency as the signal). $R_{\rm calc}$ is for no oscillation hypothesis. See text for notation.

Period	1998		1999-I		1999-II		2000	
Reactor	on	890 m off	on	750 m off	on	890 m off	on	890 m off
Duration (d)	30.4	29.4	68.2	21.8	60.4	29.6	83.2	27.5
efficiency (%)	8.0	8.0	11.5	11.6	11.6	11.6	10.9	10.8
N (d^{-1})	39.6 ± 1.1	34.8 ± 1.1	54.9 ± 0.9	45.1 ± 1.4	54.2 ± 0.9	49.4 ± 1.3	52.9 ± 0.8	43.1 ± 1.3
N' (d^{-1})	25.1 ± 0.9	21.8 ± 0.9	33.4 ± 0.7	32.0 ± 1.2	32.5 ± 0.7	32.6 ± 1.0	30.2 ± 0.6	30.4 ± 1.1
$(1-\epsilon_1)B_{\rm pn}$ (d^{-1})	0.88	0.89	1.11	1.11	1.11	1.11	1.07	1.07
Background (d^{-1})	292 ± 11	255 ± 10	265 ± 6	266 ± 10	256 ± 6	265 ± 9	249 ± 5	272 ± 9
R_ν (d^{-1})	202 ± 19	182 ± 18	212 ± 10	124 ± 17	214 ± 11	161 ± 15	237 ± 10	129 ± 16
$R_{\rm calc}$ (d^{-1})	216	154	218	129	220	155	218	154

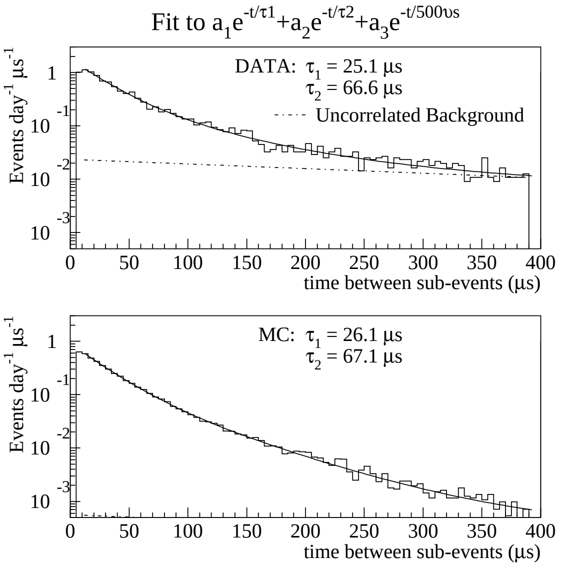

FIG. 24. Time elapsed between the prompt and delayed parts of events in PALO VERDE data and Monte Carlo. The simulated data are fit to two exponentials. Real data are fit to three exponentials of which the third accounts for the random background.

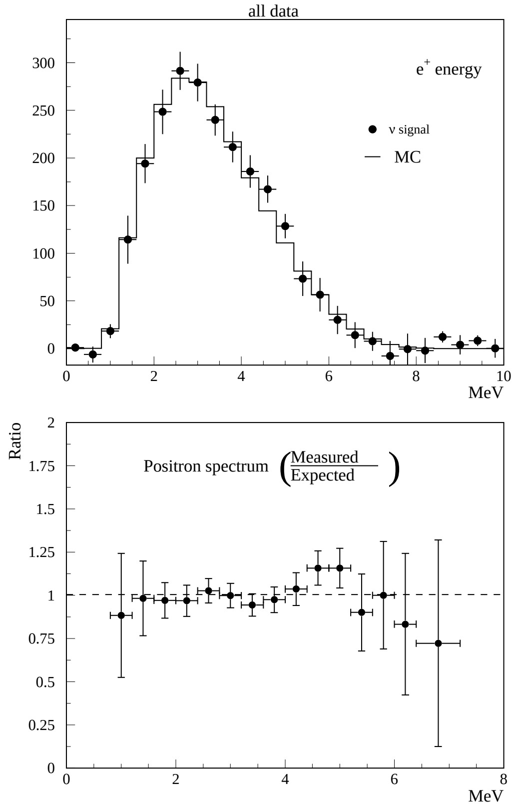

FIG. 26. Background-subtracted positron energy spectrum in CHOOZ data. Error bars represent statistical errors only. The solid histogram represents the expectation for the case of no oscillations. The ratio between the two curves is shown on the bottom panel.

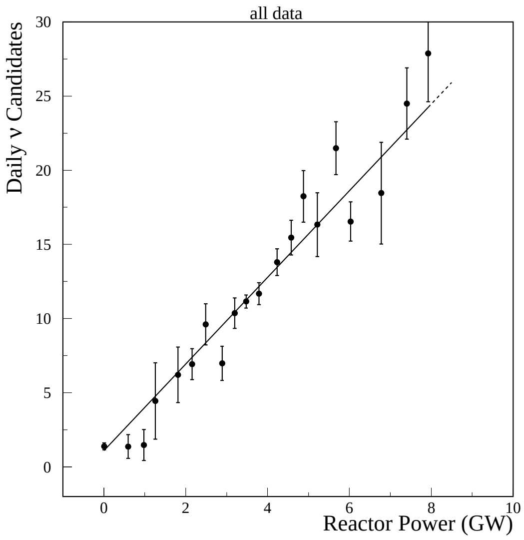

FIG. 25. CHOOZ $\bar{\nu}_e$ rate during the reactors commissioning. The background at reactors off is 1.1 ± 0.25 events/day.

The same procedure can be repeated for PALO VERDE using the thermal power excursions due to refueling. However in this case this technique substantially magnifies the errors since: 1) the periods of low power still have about 2/3 of the full flux, so that in the subtraction most of the signal is lost, 2) the statistical errors are dominated by the relatively short periods of low power. In addition, for any experiment, the background subtraction method will give correct result only if special attention is paid to the data quality, guaranteeing in particular that the efficiencies for signal *and* background are accurately known and remain as constant as possible through the experiment.

An alternative method (Wang *et al.* 2000) was developed for the PALO VERDE analysis starting from the evidence that, for their depth and detector configuration, the dominant correlated background has at least two neutrons, each triggering the detector with its capture. Such intrinsic symmetry can be used to cancel most of the background directly from data and compute the remaining components from Monte Carlo simulations. This technique makes the best possible use of the statistical power of all data collected. The rate of candidate events after all cuts can be written as $N = B_{\rm unc} + B_{\rm nn} + B_{\rm pn} + S_\nu$ where the contribution of the uncorrelated $B_{\rm unc}$, two-neutron $B_{\rm nn}$ and other correlated backgrounds $B_{\rm pn}$ are explicitly represented, along with the $\bar{\nu}_{\rm e}$ signal S_ν. The dominant background $B_{\rm nn}$ (along with $B_{\rm unc}$) is symmetric under exchange of subevents, so that an event selection with the requirements for the prompt and delayed event parts swapped, will result in a rate $N' = B_{\rm unc} + B_{\rm nn} + \epsilon_1 B_{\rm pn} + \epsilon_2 S_\nu$. Here ϵ_1 and ϵ_2 account for the different efficiency for selecting asymmetric events after the swap. One can then calculate $N - N' = (1-\epsilon_1)B_{\rm pn} + (1-\epsilon_2)S_\nu$ where the efficiency correction $\epsilon_2 \simeq 0.2$ can be estimated from the $\bar{\nu}_{\rm e}$ Monte Carlo simulation.

The PALO VERDE group found that the processes of μ-spallation in the laboratory walls and capture of the μ's that are not tagged by the veto counter, contribute to $(1-\epsilon_1)B_{\rm pn}$, while other backgrounds are negligible. Using Monte Carlo simulation, they obtain $(1-\epsilon_1)B_{\rm pn} = -0.9 \pm 0.5$ d^{-1} (-1.3 ± 0.6 d^{-1}) for μ-spallation in the 1998 (1999) data-set; the same figures for μ-capture are 0.6 ± 0.3 d^{-1} (0.9 ± 0.5 d^{-1}) in 1998 (1999). This represents only a small correction to $N - N'$ since the error on $B_{\rm pn}$ is reduced by the fact that ϵ_1 is close to 1. While the Monte Carlo model is accurate for the capture process, in the case of spallation the broad range of spectral indexes for the n-recoil energy reported in literature was simulated (Wang *et al.* 2000). The average between different predictions is then used for $B_{\rm pn}$ while the spread is used as an extra systematic error. Since no $\bar{\nu}_{\rm e}$ signal is present above 10 MeV, the observed integrated rate above such energy is used as a normalization of the Monte Carlo. The rate of neutrons produced by muon spallation has been measured at PALO VERDE (Boehm *et al.* 2000c) and the dependence of the neutron spallation yield on depth has been analyzed by Wang *et al.* (2001).

The PALO VERDE results obtained in this way are shown in Table IV for different running periods. Clearly also in this case there is good agreement with the no-oscillation hypothesis.

D. Event reconstruction techniques

The identification of the neutrino signal and the rejection of the background in reactor neutrino experiments depends on the accuracy of the event energy and position determinations and on the spatial and time correlations of the detected positron and neutron. Event reconstruction in a segmented detector like PALO VERDE is relatively simple. However, event characterization in single vessel detectors, like CHOOZ or KAMLAND, which are viewed by photomultipliers placed at the vessel surface, requires refined reconstruction methods making the best use of the PMT charge and time information. The relative importance of the time and charge information in optimizing the detector spatial resolution (which also affects the energy resolution) depends on several factors: the size of the vessel, the distance between PMTs and the fiducial target volume, the scintillator light yield and attenuation length. In CHOOZ, the relatively small detector volume and the small distance between the neutrino target and the PMTs, made the charge information the dominant one in the precise event characterization. In the case of larger volume detectors, filled with non Gd loaded scintillator, like KAMLAND (Alivisatos *et al.* 1998), or also, like the solar neutrino experiment BOREXINO (Alimonti *et al.* 1998, 2000), the time information gains importance.

As an example of a minimization algorithm for event reconstruction, based on the PMT measured charge, we describe the one used for CHOOZ. The standard algorithm uses a maximum likelihood method to reconstruct the energy E and the vertex $\vec{x}$ of an event. The likelihood is defined as the joint Poissonian probability of observing a measured distribution of photoelectrons over 24 "patches", each grouping 8 adjacent PMTs, for given $(E, \vec{x})$ coordinates in the detector. So, for an event occurring at time t after the start of data taking, one can build a likelihood function as follows:

$$\mathcal{L}(N;\overline{N}) = \prod_{j=1}^{24} P(N_j;\overline{N}_j(E,\vec{x},t)) = \prod_{j=1}^{24} \frac{\overline{N}_j^{N_j}}{N_j!} e^{-\overline{N}_j} , \tag{33}$$

where N_j is the observed number of photoelectrons and $\overline{N}_j$ the expected one for the j-th patch given an event $(E, \vec{x}, t)$. The reason for using a Poissonian instead of Gaussian statistics is due to the frequent occurrence of low energy events with low number of photoelectrons detected by some PMT patches. The predicted number of photoelectrons for each patch is computed by considering a local deposit of energy, resulting in a number of visible photons which are tracked to each PMT through the different attenuating Region 1 (Gd-doped) and Region 2 scintillators. Therefore

$$\overline{N}_j = \alpha E \eta \sum_{k=1}^{8} \frac{\Omega_{jk}(\vec{x})}{4\pi} \exp\left(-\frac{d_1^{jk}(\vec{x})}{\lambda_{Gd}(t)} - \frac{d_2^{jk}(\vec{x})}{\lambda_{Hi}}\right) \tag{34}$$

where E is the ionization energy deposited in the scintillators, α is the light yield of the scintillator, η is the average PMT quantum efficiency, Ω_{jk} is the solid angle subtended by the k-th PMT from the event position, d_1^{jk} is the light path length in region 1, d_2^{jk} is the light path length in region 2, λ_{Gd} is the attenuation length in region 1 scintillator, and λ_{Hi} is the attenuation length in region 2 scintillator.

The solid angle is approximated by the expression

$$\Omega_{jk} = 2\pi \left(1 - \frac{d_{jk}}{\sqrt{d_{jk}^2 + r_{PMT}^2 \cos\theta}}\right) \quad (35)$$

r_{PMT} being the PMT photocathode radius, $d_{jk} = d_1^{jk} + d_2^{jk}$, and θ being the angle between the event-PMT direction and the inward unit vector normal to the PMT surface.

Instead of (33), as is usually the case for problems involving the maximum likelihood method, it is more convenient to use the theorem on the "likelihood ratio test" for goodness-of-fit to convert the likelihood function into the form of a general χ^2 statistics (Eadie *et al.* 1971). If one assumes N_j to be the best estimate of the true (unknown) photoelectron distribution and can form the likelihood ratio λ defined by

$$\lambda = \frac{\mathcal{L}(N;\overline{N})}{\mathcal{L}(N;N)} \quad (36)$$

The "likelihood ratio test" theorem states that the "Poissonian" χ^2, defined by

$$\chi^2 = -2\log\lambda = 2\sum_{j=1}^{24}[\overline{N}_j - N_j + N_j \log(\frac{N_j}{\overline{N}_j})], \quad (37)$$

asymptotically obeys a chi-square distribution (Baker and Cousins 1984). It is easy to prove that the minimization of χ^2 is equivalent to maximization of the likelihood function, so that the χ^2 statistic may be useful both for estimating the event characteristics and for goodness-of-fit testing.

The CERN-MINUIT package (James 1994) was used to minimize (37). The starting value for the i-th coordinate was based on the charge asymmetries measured by initially grouping the PMTs into only 6 "superpatches", referred to the detector frame axes; it was defined according to:

$$x_{i0} = \frac{\sqrt{Q_+^i} - \sqrt{Q_-^i}}{\sqrt{Q_+^i} + \sqrt{Q_-^i}} D^i, \quad i = 1,2,3, \quad (38)$$

where the indices $+-$ refer to the opposite superpatches of the i-th axis and D^i is the half size of the detector along that axis. Once the x_{i0} corresponding to the starting position is known, the starting energy value is obtained from (34) after replacing $\vec{x}$ with $\vec{x}_0$ and $\overline{N}_j$ with N_j. Examples of the results obtained by this procedure are shown in Fig. 17.

E. Results and systematics

A summary of systematic errors for both CHOOZ and PALO VERDE is given in Table V. The systematic error given for CHOOZ should probably be considered as some sort of ultimate limit for reactor-based oscillation experiments, at least when only one detector is present. Indeed the intrinsically high efficiency ($\simeq 70\%$) of the homogeneous detector, together with the unique opportunity of studying the zero power case, are important advantages (for comparison the efficiency of the larger but segmented PALO VERDE detector is $\simeq 11\%$).

The (energy averaged) ratio between $\bar{\nu}_e$ detected and expected was found to be

$$R = 1.01 \pm 2.8\%(\text{stat}) \pm 2.7\%(\text{syst}) \qquad \text{CHOOZ} \quad (39)$$

and

$$R = 1.01 \pm 2.4\%(\text{stat}) \pm 5.3\%(\text{syst}) \qquad \text{PALO VERDE} \quad (40)$$

in both cases consistent with unity.

TABLE V. Origin and magnitude of systematic errors in PALO VERDE and CHOOZ. Note that the two experiments offer different breakdowns of their systematics. For simplicity we do not show the systematics for the PALO VERDE ON-OFF analysis. The PALO VERDE results are from the analysis of the full data set (Boehm *et al.* 2001).

Systematic	CHOOZ (%)		PALO VERDE (%)	
$\sigma(\bar{\nu}_e + p \rightarrow n + e^+)$	1.9		-	
Number of p in target	0.8		-	
W_{th}	0.7		-	
Energy absorbed per fission	0.6		-	
Total rate prediction		2.3		2.1
e^+ trigger eff.	-		2.0	
n trigger eff.	-		2.1	
$\bar{\nu}_e$ selection cuts	-		2.1	
$(1-\epsilon_1)B_{pn}$ estimate	-		3.3	
Total $\bar{\nu}_e$ efficiency		1.5		4.9
Total		2.7		5.3

Both experiments were able to exclude $\bar{\nu}_e$ - $\bar{\nu}_x$ oscillations as dominating for the atmospheric neutrino anomaly. This is evident from the exclusion contours obtained using the unified approach (Feldman and Cousins 1998) and shown in Figure 27 for CHOOZ and Figure 28 for PALO VERDE.

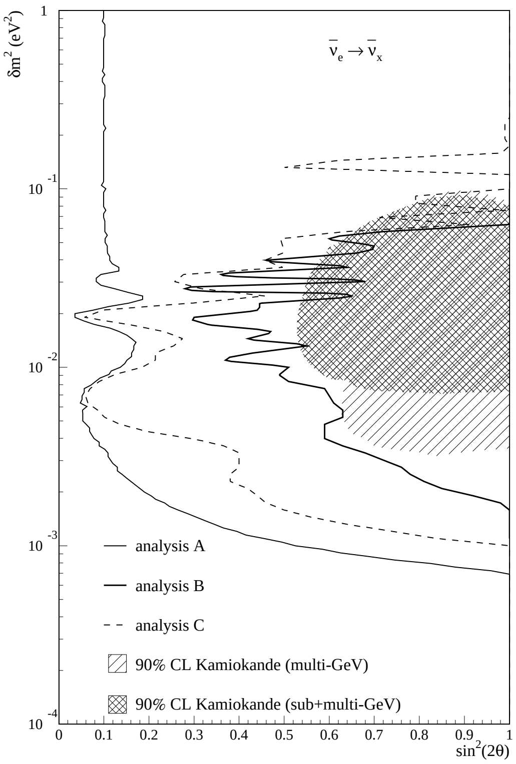

FIG. 27. Limits on mass difference and mixing angle from CHOOZ (90% CL) obtained with the unified approach (Feldman and Cousins 1998). Analysis A refers to the curve obtained by a fit to the background-subtracted spectrum in which both shape and normalization are used. Analysis C uses only the shape of the spectrum. Finally analysis B uses the difference of baselines between the two reactors ($\Delta L = 116.7$ m). While in this last case most systematics cancel, statistical errors are larger and the Δm^2 sensitivity rather poor due to the short baseline difference. The Kamiokande $\nu_e - \nu_\mu$ atmospheric neutrino result is also shown.

F. Are smaller mixing angles within experimental reach ?

The current data on neutrino oscillations suggests the need to include at least three neutrino flavors when studying results from experiments. As discussed in the Introduction, the most general approach would involve five unknown parameters, three mixing angles and two independent mass differences. However, an intermediate approach consists of a simple generalization of the two flavor scenario, assuming that $m_3^2 \gg m_1^2, m_2^2$ (i.e. $\Delta m_{13}^2 = \Delta m_{23}^2 = \Delta m^2$, while $\Delta m_{12}^2 \simeq 0$). This scenario is obviously compatible with the evidence based on the atmospheric neutrino anomaly ($\Delta m^2 \sim 3 \times 10^{-3}$ eV^2) and the solar neutrino deficit ($\Delta m^2 < 10^{-4}$ eV^2). In such a case the mixing angle θ_{12} becomes irrelevant and one is left with only three unknown quantities: $\Delta m^2, \theta_{13}$, and θ_{23}. With this parameterization, and assuming that ν behave like $\bar{\nu}$, the $\bar{\nu}_e$ disappearance is governed by

$$P(\bar{\nu}_e \rightarrow \bar{\nu}_x) = \sin^2 2\theta_{13} \sin^2 \frac{\Delta m^2 L}{4E_\nu} \ , \qquad (41)$$

while $\nu_\mu \rightarrow \nu_\tau$ oscillations, in this scenario responsible for the atmospheric neutrino results, are described by

$$P(\nu_\mu \rightarrow \nu_\tau) = \cos^4 \theta_{13} \sin^2 2\theta_{23} \sin^2 \frac{\Delta m^2 L}{4E_\nu} \ . \qquad (42)$$

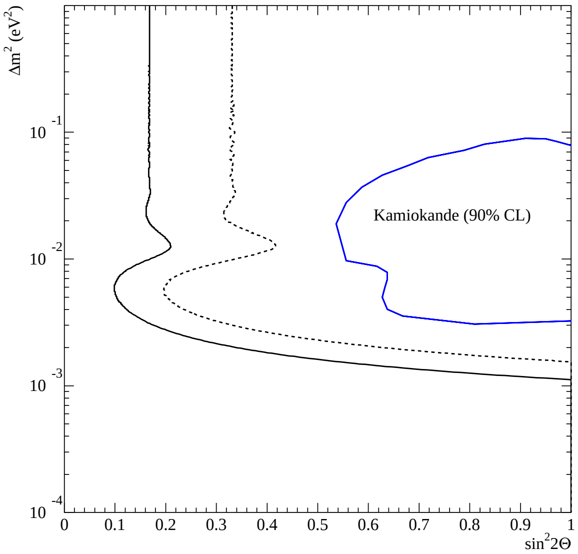

FIG. 28. Limits on mass difference and mixing angle from PALO VERDE at 90% CL (Boehm *et al.* 2001). The full curve is obtained with the *swap* background subtraction method described in the text, while the dashed is obtained using the reactor power changes to estimate and subtract the background. The Kamiokande $\nu_\mu - \nu_e$ atmospheric neutrino result is also shown for illustration.

An analysis of the atmospheric neutrino data based on these assumptions has been performed (Okamura 1999) and its results are shown in Figure 29 for the ν_e disappearance channel. One can see that, while the relevant region of the mass difference Δm^2 is determined by the atmospheric neutrino data, the mixing angle θ_{13} is not constrained very much. Here the reactor-based neutrino oscillation experiments play a decisive role.

The determination of the angle θ_{13} has obvious importance not only for the structure of the lepton mixing matrix U but for the observability of CP violation in the lepton sector, as stressed in the Introduction. If θ_{13} vanishes, or is very small, no CP violation effects are observable in the lepton sector. Moreover, for the vanishing θ_{13} and with three neutrinos only, the lepton mixing is radically simplified. The electron neutrino is then simply

$$\nu_e = \cos\theta_{12}\nu_1 + \sin\theta_{12}\nu_2 \ , \tag{43}$$

while the ν_μ and ν_τ neutrinos become superpositions of ν_3 and the corresponding orthogonal combination of ν_1 and ν_2. It is therefore interesting to ask whether reactor-based experiments can be extended to address regions of even smaller mixing parameter $\sin^2 2\theta_{13}$.

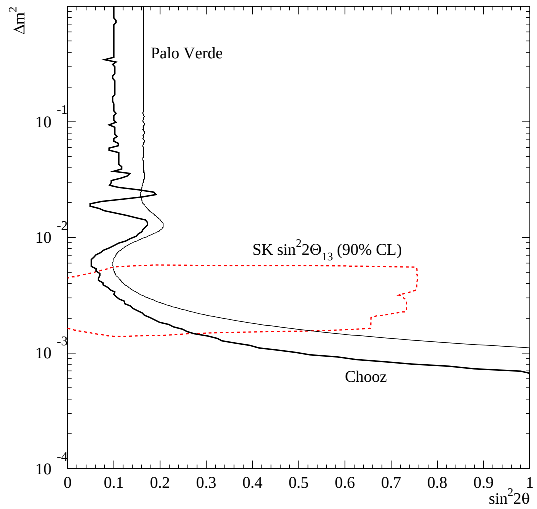

FIG. 29. Exclusion plot showing the *allowed* region of θ_{13} and Δm^2 based on the Super-Kamiokande preliminary analysis (the region *inside* the dotted curve). The region *excluded* by the neutrino reactor experiments are to the right of the corresponding thick and thin continuous curves.

A simple inspection of Table V shows that, using the Chooz systematics, if all flux and cross-sections related errors could be set to zero one would be left with an error of $\simeq 1.5\%$. Hence, assuming a detector large enough to produce negligible statistical error the total error would shrink from the present 3.9% to 1.5%.

This scenario is considered by Mikaelyan (2000) that proposes to use an underground reactor at Krasnoyarsk in Russia as a source and two identical detectors placed at distances of $\simeq 1100$ m and $\simeq 250$ m. The interesting feature of the Krasnoyarsk site is that there are substantial facilities available underground, with an overburden of ~ 600 m.w.e., twice the depth of Chooz. Indeed it might even be conceivable to locate the detectors on rail-cars and periodically switch their position to further reduce some of the systematics related to detector efficiency. The proposal discusses the use of 50 tons of Gd-loaded scintillator for each of the two identical homogeneous detectors, so that the far detector would collect 50 events/day (the thermal power of the reactor is in this case lower than at Chooz or Palo Verde). The background is estimated by Mikaelyan (2000) to be of 5 events/day or less.

This proposal estimates that such an experiment could reach a sensitivity in mixing strength of better than 0.02 in the Δm^2 region relevant for atmospheric neutrinos. While the idea looks certainly interesting, it would be useful to explore how practical it is in general to push the errors of the absolute $\bar{\nu}_e$ flux to the 1% domain, even with the measurements considered here. Note also that the Krasnoyarsk reactors, according to the Gore-Chernomyrdin[‡‡] agreement, are supposed to be shutdown for re-coring in not very distant future.

V. EXPLORING THE SOLAR ν ANOMALY ON EARTH: KAMLAND

While historically solar neutrinos provided the first hint for oscillations, there is a consensus today that the strongest evidence for oscillation is the atmospheric neutrino anomaly. Indeed, the zenith angle dependence of the anomaly has substantially helped to eliminate explanations not based on some property of neutrinos themselves and the advent of K2K, to be followed soon by the Minos and CERN to Gran Sasso programs (Wojcicki 2001a, 2001b), are bringing the study of oscillations in this regime to a laboratory activity with both source and detector well under control.

In the case of solar neutrinos none of the effects that would be generally considered "smoking guns" for oscillations has yet clearly emerged from the data and their exploration "in a laboratory setting" is made particularly challenging by the huge L/E_ν required. It is probably a safe prediction that it will take a very long time before an accelerator-based experiment will be able to tackle the solar neutrino problem! However, the very low energy of reactor neutrinos make a reactor-based oscillation experiment able to reach the Large Mixing Angle (LMA MSW) solution possible - albeit rather challenging. While the analysis of current and future solar neutrino experiments presumably will help to decide which of the

[‡‡] "US-Russian Plutonium Production Agreement is Signed" Statement by the White House office of the Vice President, 23 Sept. 1997.

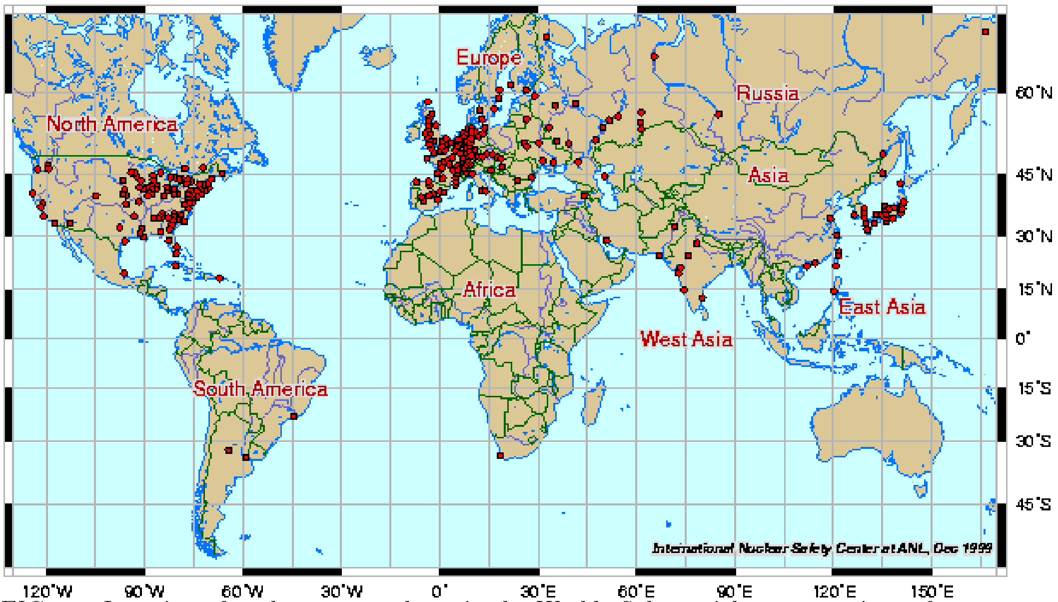

FIG. 30. Location of nuclear power plants in the World. Substantial concentrations of reactors are in Europe, East of the US and Japan. (Note that the map, see http://www.insc.anl.gov/, contains few plants that were either planned but never built or are no longer operational.)

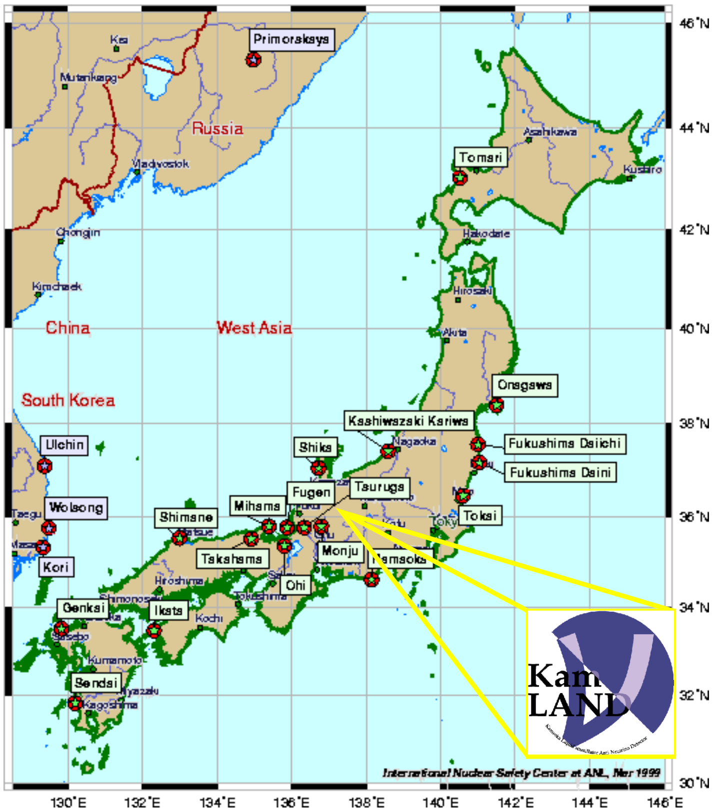

FIG. 31. Location of large nuclear power plants in Japan, Korea and Far East Russia. (See the comment in the caption of Fig. 30.)

possible solutions is the right one, we find the chance to study solar neutrino oscillations "in the lab" extremely compelling. Note that, unlike in the case of atmospheric neutrinos, where it turned-out that electron neutrinos are not involved in the dominant mixing, the solar neutrino problem, if due to oscillations, obviously involves ν_e disappearance. So, unless $\bar{\nu}_e$ behave drastically differently from ν_e (which would be a worthwhile discovery anyway, signaling the breakdown of CPT symmetry) a reactor experiment is an exact replica of the astrophysical experiment, only built on earth.

A. Nuclear reactors in Japan

The "easier" solution of the solar neutrino problem (MSW LMA) is shown in Figure 1. In order to completely explore such solution one needs a Δm^2 sensitivity of at least 10^{-5} eV^2 at large mixing angle. As now customary we refer to Figure 3 as a first step in designing our experiment: we see that a $\approx$ 100 km baseline is needed and this drives the power$\times$fiducial-mass product in the 10^8 MW$_{th}\times$tons range. Clearly a large detector has to be used in conjunction with very many nuclear reactors. A cursory look at the placement of nuclear power plants on the earth, Figure 30, reveals that such an experiment could only be placed in Europe, East of the United States, or Japan.

There are 16 commercial nuclear power plants in Japan, their location being shown in Figure 31. They supply about 1/3 (or 130 GW$_{\rm th}$) of the total electric power in the country. At the Kamioka site there is an anti-neutrino flux of $\simeq 4\times10^6$cm^{-2}s^{-1} (or $\simeq 1.3\times10^6$cm^{-2}s^{-1} for $E_{\bar{\nu}} > 1.8$MeV) from these reactors. 80% of such flux derives from reactors at a distance between 140 km and 210 km, so that there is a limited range of baselines. The breakdown of this data by power plant (several plants have on site more than one reactor) is given in Figure 32. We note that some 2% of the flux derives from power plants in South Korea (the Primorskaya plant in Russia is only planned) that will have to be included (albeit only as a crude estimate) to provide an exact flux prediction.

While the Figure 32 assumes the nominal power for each of the cores, an average over one year, taking into account scheduled and unscheduled down times, gives an expected non-oscillation rate of $\simeq$750 kton^{-1}year^{-1} for a C_nH_{2n+2} target. Although the signal is provided by a very large number of cores it turns out that a modulation of the $\bar{\nu}_e$ flux is expected at KamLAND (Alivisatos *et al.* 1998) thanks to the refueling and maintenance schedule of nuclear power plants in Japan. Such shutdowns, in fact, are concentrated in the Fall and Spring when the power demand is lowest, as illustrated in Figure 33. Hence, from the point of view of the tools available to study backgrounds, KamLAND is in a situation very similar to that of Palo Verde, with 2 dips in the flux from full to $\approx 2/3$ expected every year.

Site	Distance (km)	# of cores	P(ther.) (GW)	flux ($\bar{\nu}$ cm^{-2}s^{-1})	Signal ($\bar{\nu}$/yr)
Japan					
Kashiwazaki	160.0	7	24.6	4.25×10^5	348.1
Ohi	179.5	4	13.7	1.88×10^5	154.0
Takahama	190.6	4	10.2	1.24×10^5	101.8
Hamaoka	214.0	4	10.6	1.03×10^5	84.1
Tsuruga	138.6	2	4.5	1.03×10^5	84.7
Shiga	80.6	1	1.6	1.08×10^5	88.8
Mihama	145.4	3	4.9	1.03×10^5	84.5
Fukushima-1	344.0	6	14.2	5.3×10^4	43.5
Fukushima-2	344.0	4	13.2	4.9×10^4	40.3
Tokai-II	294.6	1	3.3	1.7×10^4	13.7
Shimane	414.0	2	3.8	9.9×10^3	8.1
Onagawa	430.2	2	4.8	9.8×10^3	8.1
Ikata	561.2	3	6.0	8.4×10^3	6.9
Genkai	755.4	4	6.7	5.3×10^3	4.3
Sendai	824.1	2	3.3	3.5×10^3	2.8
Tomari	783.5	2	5.3	2.4×10^3	2.0
Korea					
Ulchin	~750	4	11.2	8.8×10^3	7.2
Wolsong	~690	4	8.1	7.5×10^3	5.2
Yonggwang	~940	6	16.8	8.4×10^3	6.9
Kori	~700	4	8.9	8.0×10^3	6.6
Total		**69**	**175.7**	**1.34×10^6**	**1102**

FIG. 32. List of relevant parameters for power reactors in Japan and South Korea.

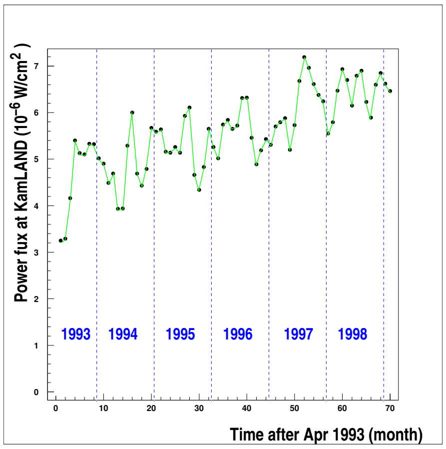

FIG. 33. Power-flux level at Kamioka from Japanese reactors as function of time. Low power periods in the Fall and Spring seasons are alternated with peaks of high power in the Summer and Winter.

It is interesting to remark that other artificial sources of low energy $\bar{\nu}_e$ are not a serious background in KamLAND. The largest effect would be produced by a large nuclear powered vessel stationed, while running its reactors at full power, in the Toyama bay, 50 - 100 km from the detector. In these circumstances the excess signal in KAMLAND would amount to ~10% (Detwiler 2000). It is clear that it is extremely unlikely that such conditions will occur for any significant period of time.

B. Detector design

The KAMLAND detector is housed in the cavity built for the Kamiokande detector under the summit of Mt. Ikenoyama in the Japanese Alps, about 50 km east of the town of Toyama. The layout of the laboratory is shown in Figure 34. The rock overburden is more than 1,000 m in any direction with an average rock density of 2.7 g/cm^3. The site is at 500 m distance from SuperKamiokande.

A cutout view of the KAMLAND detector is shown in Figure 35. The fiducial volume consists of a sphere containing 1000 tons of liquid scintillator. The scintillator container is a thin plastic-walled balloon of 6.5 m radius that is not supposed to take the weight of the scintillator but only to isolate it from an outer 2.5 m thick layer of non-scintillating, radiation shielding, fluid. The balloon is also designed to be impermeable to radon that mainly originates from Th and U contaminations inside the PMT's glass. The buffer fluid and the liquid scintillator are contained and mechanically supported by a stainless steel spherical vessel that also provides the mechanical structure where the photomultipliers for the fiducial volume are mounted. The sphere is solidly anchored inside the cylindrical rock cavity and the space between them is filled with water and used as a veto Čerenkov counter. The scintillator, based on mineral oil and pseudocumene, is designed to achieve sufficient light yield and n-γ discrimination by pulse-shape analysis, yet complying with rather strict flammability requirements from the Kamioka mine. Given the cost and stability issues for a detector of the size of KAMLAND, it was chosen not to Gd-load the scintillator. As it will be discussed later, simulations indicate that sufficient signal-to-noise ratio will be achieved with unloaded scintillator. Events will be localized inside the fiducial volume using the light intensity and propagation delays to the different photomultipliers so that large area, fast tubes are required. While the veto counter will be read-out using 20-inch photomultipliers dismounted from the Kamiokande detector, new, faster, tubes with 17-inch active photocathode have been developed for KAMLAND in order to allow for proper vertex reconstruction from timing. Such tubes have an average transit-time-spread of $\simeq$ 3 ns (to be compared to $\simeq$ 5 ns for the Kamiokande/SuperKamiokande tubes). The central detector has a 30% photocathode coverage obtained using about 1280 seventeen-inch tubes complemented, for energy measurements, by 642 twenty-inch Kamiokande tubes. A spherical shell of acrylic panels (not shown in Figure 35) is mounted at a radius immediately inside the position of the PMT's and is used as primary barrier against radon migration into the active scintillator. A cylindrical stainless steel chimney of 3 m diameter protrudes from the top of the sphere to permit access to the central detector during installation. Buffer fluid and scintillator lines as well as calibration ports are mounted in the chimney along with all the electrical cabling.

The readout of KAMLAND is designed to provide waveform analysis information for each of the PMT's in the detector with essentially no dead-time for several consecutive events. This allows for clean event reconstruction and enables the off-line study of the pre-history of interesting events. For example multiple neutron events, described above as the most dangerous background at PALO VERDE, will be fully reconstructed by KAMLAND. Similarly cosmogenic activation giving short half-life nuclei will be clearly recorded. Deep digital buffering will allow the detector to sustain substantial burst of events like expected from supernovae.

In Figure 36 we show a phase of the central detector PMT installation that was concluded in September 2000. Scintillator filling started in Spring 2001 and data taking at KAMLAND is scheduled to begin before the end of 2001.

C. Expected performance

Similarly to previous experiments, both random hits from natural radioactivity and correlated events from neutron production in cosmic-ray-muon spallation and capture, contribute to the background to reactor $\bar{\nu}_e$ in KAMLAND. The results of Monte Carlo full detector simulation using the measured Kamioka cosmic ray flux and the activities of various components as sampled during construction are given in Table VI. For the purpose of this background estimate U and Th contaminations in the scintillator of 10^{-14} g/g has been assumed. Such purity level has been already achieved in samples of the KAMLAND scintillator. Monte Carlo studies have shown that cosmogenic activation gives negligible contribution to the background for doubles. A discussion of backgrounds to single signatures, not considered here, can be found in Alivisatos *et al.* (1998).

TABLE VI. Summary of background rates in KAMLAND for the $\bar{\nu}_e$ signature. A signal-to-noise ratio of about 10/1 is expected for reactor $\bar{\nu}_e$. Adapted from Alivisatos *et al.* (1998).

Background source	Rate (day^{-1})
Cosmic muons induces neutrons	0.1
Natural radioactivity (random coincidence)	0.15
Natural radioactivity (correlated)	0.005
Total predicted background	0.25
Reactor $\bar{\nu}_e$ signal (no oscillation)	2

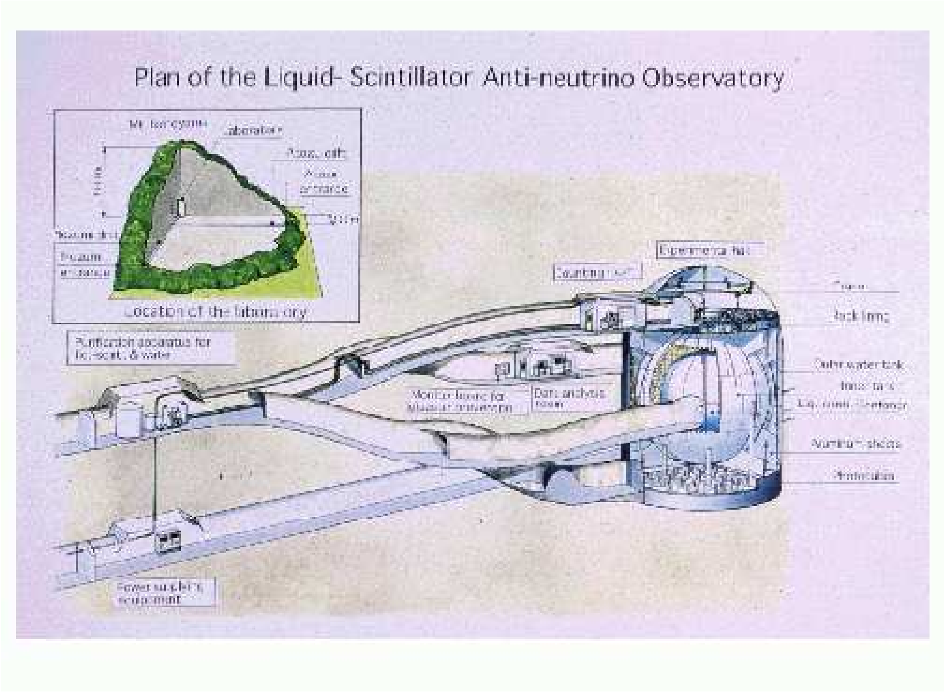

FIG. 34. Partial view of the system of tunnels inside Mount Ikenoyama with the locations of KamLAND and its main services.

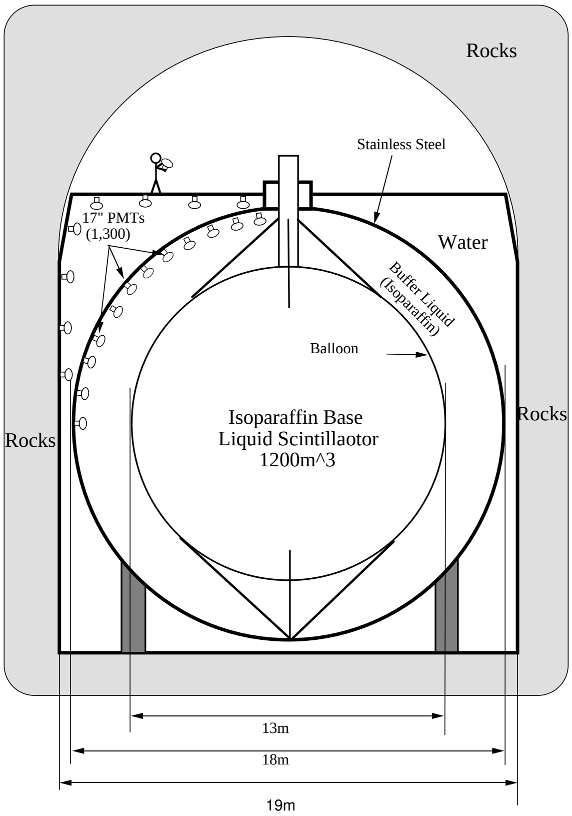

FIG. 35. Schematic cross-section of the KamLAND detector.

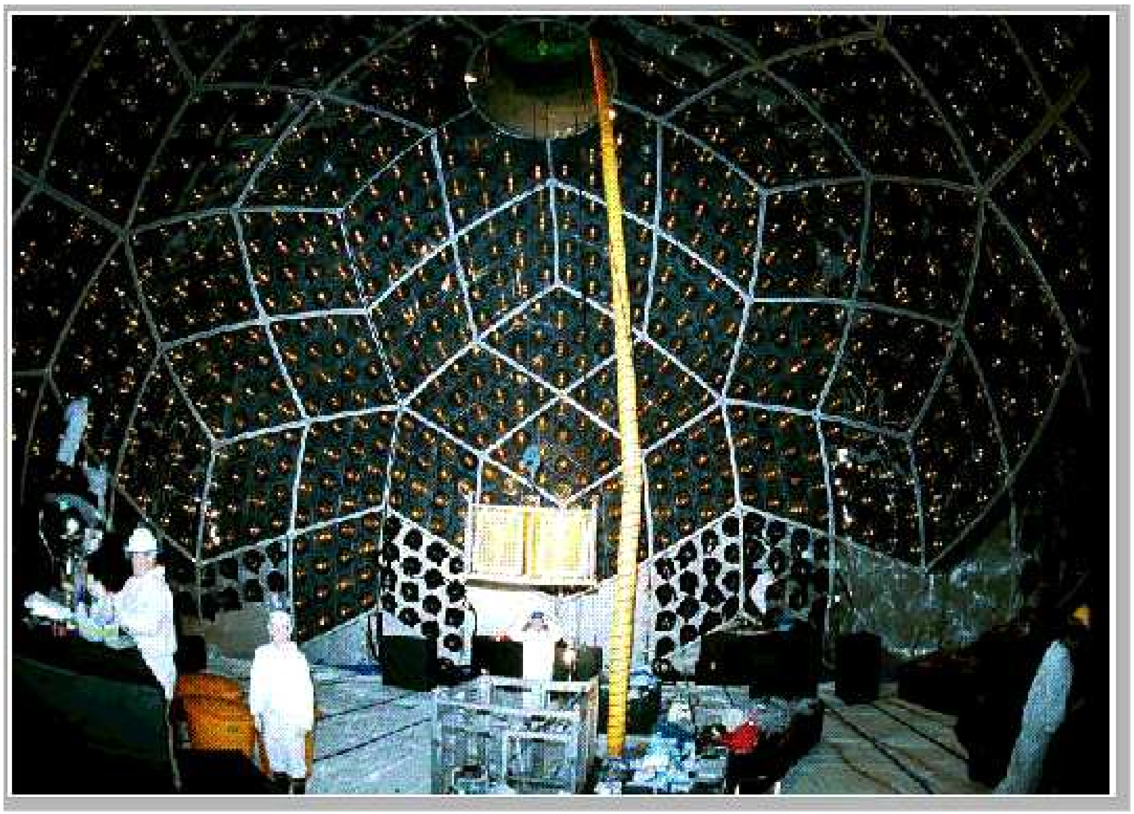

FIG. 36. View of the internal volume of the KAMLAND sphere during the central detector installation. A modular styrofoam raft is used as a platform for workers. The installation begun from the top of the sphere and moved down, as the water level in the sphere was reduced. PMTs, black shades, acrylic plates, monitoring LEDs and cables were mounted in place for each level before lowering the water.

In Figure 37 we show the predicted energy spectra for reactor neutrinos at KamLAND for no oscillations and different oscillation parameters consistent with the LMA MSW solar neutrino solution. We can use one of such curves and add to it fluctuations consistent with a 10/1 signal-to-noise ratio and three years of data to investigate the sensitivity of the experiment. Assuming that oscillations with $\Delta m^2 = 2 \times 10^{-5}$ eV^2 and $\sin^2 2\theta = 0.75$ are indeed the cause of the solar neutrino anomaly, we obtain the measurement of the oscillation parameters shown in Figure 38. On the other hand, no evidence for oscillation after three years of data would result in the exclusion curve shown in Figure 1 and would rule-out the LMA MSW solution to the solar neutrino problem.

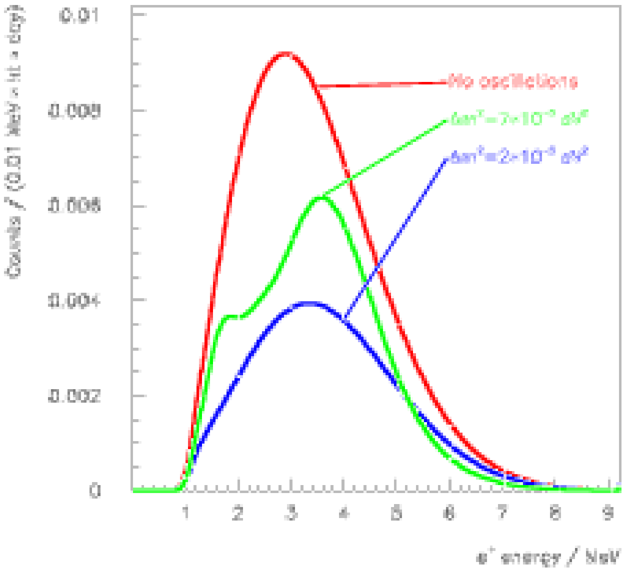

FIG. 37. Positron energy spectra expected at KamLAND for no oscillations and oscillations with indicated parameters Δm^2 and $\sin^2 2\theta = 0.75$ in the MSW LMA solar neutrino solution.

D. Other physics with a very large low-energy $\bar{\nu}_e$ detector

KamLAND will be the largest detector specifically optimized to detect low-energy $\bar{\nu}_e$ with good efficiency and low background. This opens a number of interesting opportunities beyond the measurement of oscillations from reactors. In addition, such a large detector with a low energy threshold can be used to directly measure neutrinos from the sun, assuming that backgrounds can be sufficiently reduced and understood to enable the detection of single energy deposits. Of particular importance is the ^{7}Be line that is below the threshold of the water Čerenkov detectors. The presence of large amounts of carbon in KamLAND's scintillator opens the possibility of detailed flavor studies in neutrinos coming from supernovae. Finally KamLAND represents such a large step in size and backgrounds relative to the previous detectors that one should be ready for the possibility that it will discover completely new and un-expected phenomena in physics or astrophysics.

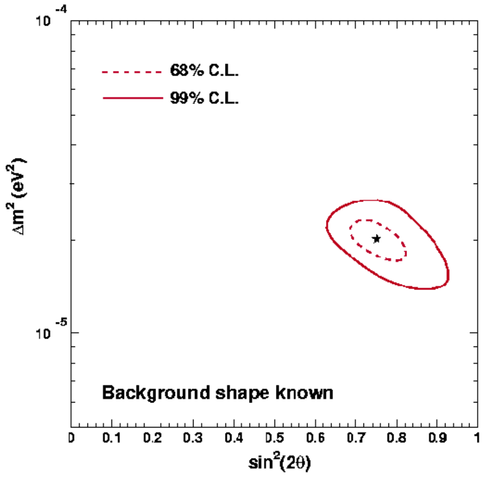

FIG. 38. Simulated measurement of neutrino oscillation parameters from three years of data at KamLAND assuming $\Delta m^2 = 2 \times 10^{-5}$ eV^2 and $\sin^2 2\theta = 0.75$. A signal-to-noise ratio of 10/1 was assumed (see text).

Here we will only mention the topic of terrestrial $\bar{\nu}_e$ that is somewhat unusual and directly relates to the experiment's ability to detect $\bar{\nu}_e$. The reader interested in the direct detection of solar neutrinos or neutrinos from supernovae is referred to the KamLAND design report (Alivisatos *et al.* 1998). A description of the new and un-expected phenomena mentioned above will be hopefully provided at a later stage.

Although the study of terrestrial anti-neutrinos was proposed as early as 1966 (Eders 1966) practical difficulties, due to the very small cross-sections and very low energies involved, have made this physics impractical until now. KamLAND has the ability to detect energy depositions of the order of 1 MeV in a unprecedented amount of liquid scintillator and is therefore ideally suited for this study. It is important to realize that low energy $\bar{\nu}_e$ are easily detected with very low background in KamLAND thanks to their very specific signature.

The cooling rate of our planet and its contents of heavy elements are central issues in the earth sciences. The earth radiates about 40 TW of heat from its surface. About 40% of this energy (or 16 TW) is believed to have radiogenic origin with 90% of it deriving from decays of ^{238}U and ^{232}Th. Radiogenic heat is therefore an essential component of the present Earth dynamics. As discussed by several authors (Eders 1966, Marx 1969, Marx and Lux 1970, Avilez *et al.* 1981, Krauss 1984) the concentration of these isotopes can be mapped, at planetary scale, by direct detection of $\bar{\nu}_e$ deriving from the β-decay processes. Since neutrinos have a mean free path many orders of magnitude larger that the size of the Earth, the neutrino field is analogous to a gravitational field, where the sources are represented by radioactive density (as opposed to mass density).

Since the maximum energy carried by terrestrial neutrinos is (Krauss 1984) 3.27 MeV and the capture threshold is 1.8 MeV, the maximum in the energy spectrum detected in the prompt part of the events will be 2.49 MeV (including the 1.02 MeV from positron annihilations). For energies above threshold only the Thorium and Uranium decay chains give a detectable amount of events. ^{234}Pa from the U chain and ^{228}Ac and ^{212}Bi of the Th chain have similar endpoints (respectively 2.29 MeV, 2.08 MeV and 2.25 MeV) while ^{214}Bi from the U chain has an endpoint of 3.27 MeV. Therefore the energy spectrum observed for the prompt part of the event should have a characteristic double-hump structure shown in Figure 39. This will also allow the measurement of the U/Th ratio. Anti-neutrinos from nuclear reactors give, as described above, a similar signature, but their energy is substantially higher and, as shown in the Figure, they can be easily separated from the terrestrial anti-neutrinos. Indeed, a repetition of the analysis for the reactor neutrinos discussed above using only positron energies above 2.7 MeV gives an oscillation sensitivity very similar to the one presented in Figure 38.

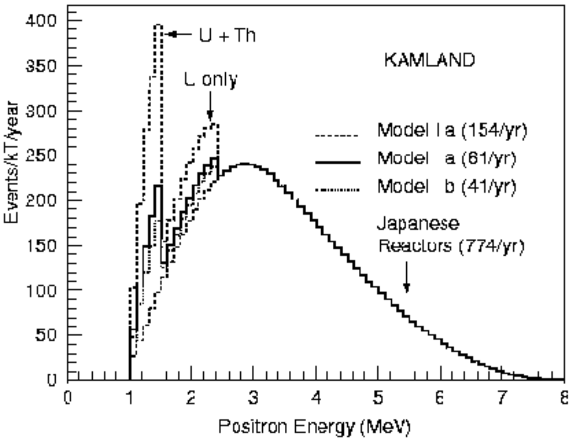

FIG. 39. Energy spectrum from terrestrial anti-neutrinos compared with reactor signal as expected in KAMLAND. Three different geophysical models are shown for the terrestrial anti-neutrinos and no oscillations are assumed for all the spectra shown. Adapted from Raghavan *et al.* (1998).

The two lower spectra (Ia and Ib) superimposed in Figure 39 for the terrestrial anti-neutrino component correspond to two different possible geophysical models with different heavy elements concentration in the oceanic and continental crusts (Raghavan *et al.* 1998). The highest curve (IIa) is given as a reference and shows what the spectrum would be in the extreme case where the entire 40 TW of heat escaping from the Earth's interior was generated by the Th and U decay chains.

In one year of data-taking, model Ia would give an integral of 61 events while model Ib would give only 41 events, and a differentiation between the two at 3σ level could be obtained in five years of data-taking, taking into account the fluctuations of the background due to the reactor neutrinos.

VI. CONCLUSIONS

The use of nuclear reactors to study neutrino properties has a long and glorious history. While the first experiments devoted to oscillation searches were motivated by the generic principle to "look where the light is", many of the modern hints for neutrino oscillations point to parameters that match very well the capabilities of reactor-based experiments. At the same time the understanding of the flux and spectrum of $\bar{\nu}_e$ from power reactors has reached substantial sophistication. The first two "long baseline" experiments, CHOOZ and PALO VERDE, have amply demonstrated the capability of this new breed of detectors, while providing solid evidence that $\nu_{\rm e} - \nu_\mu$ is *not* the dominant channel in the atmospheric neutrino oscillation. KAMLAND, scheduled to begin data-taking shortly, will extend the reach for small mass-differences to unprecedented levels. Its size and background will move reactor-based experiments to a new dimension, with several new physics opportunities in the essentially background-less detection of $\bar{\nu}_e$ from a number of natural sources.

VII. ACKNOWLEDGMENT

We would like to thank our colleagues from CHOOZ, KAMLAND and PALO VERDE for the many discussions and help received in understanding the material discussed. This work was supported in part by the US DoE and by the Italian INFN.

REFERENCES

Achkar B., 1992, Thesis, (ILL Grenoble).
Achkar B. *et al.*, 1995, Nucl. Phys. **B434**, 503.
Achkar B. *et al.*, 1996, Phys. Lett. **B374**, 243.
Ahmad Q. R. *et al.*, 2001, Phys. Rev. Lett., submitted.

Alfonin A. I. *et al.*, 1998, JETP **67**, 213.
Alimonti G. *et al.*, 1998, Astroparticle Physics **8**, 141.
Alimonti G. *et al.*, 2000, NIM **A440**, 360.
Alivisatos P. *et al.* 1998, KAMLAND: *a liquid scintillator Anti-Neutrino Detector at the Kamioka site*, preprint Stanford-HEP-98-03, Tohoku-RCNS-98-15.
Amsler C. *et al.*, 1997, Nucl. Inst. Meth. **A396**, 115.
Apollonio M. *et al.*, 1998, Phys. Lett. **B420**, 397.
Apollonio M. *et al.*, 1999, Phys. Lett. **B466**, 415.
Apollonio M. *et al.*, 2000, Phys. Rev. D **61**, 012001.
Armbruster B. *et al.*, 1998, Phys. Rev. C**57**, 3414.
Athanassopoulos C. *et al.*, 1995, Phys. Rev. Lett. **75**, 2650.
Athanassopoulos C. *et al.*, 1996, Phys. Rev. C**54**, 2685.
Athanassopoulos C. *et al.*, 1998, Phys. Rev. C**58**, 2489.
Avilez C. *et al.*, 1981, Phys. Rev. D**23**, 1116.
Bahcall J. N., 1989, *Neutrino Astrophysics*, (Cambridge Univ. Press, Cambridge).
Baldini A. *et al.*, 1996, Nucl. Instr. and Meth. **A372**,207.
Baker S. and Cousins R., 1984, Nucl. Instr. Meth. **221**, 437.
Barger V., Whisnant K., and Phillips R. J. N., 1980, Phys. Rev. Lett. **45**, 2084.
Beacom J. F. and Vogel P., 1999, Phys. Rev. Lett. **83**, 5222.
Boehm F. *et al.*, 2000a, Phys. Rev. Lett. **84**, 3764.
Boehm F. *et al.*, 2000b, Phys. Rev. D**62**, 072002.
Boehm F. *et al.*, 2000c, Phys. Rev. D**62**, 092005.
Boehm F. *et al.*, 2001, hep-ex/0107009, Phys. Rev. D, submitted.
Boehm F. and Vogel P., 1992 *Physics of Massive Neutrinos*, (Cambridge Univ. Press, Cambridge).
Boehm F., 2001, chapter in *Current aspects of Neutrino Physics*, D. Caldwell ed., (Springer, Heidelberg), to be published.
Cabibbo N., 1978, Phys. Lett. **72B**, 333.
Danby G. *et al*, 1962, Phys. Rev. Lett. **9**, 36.
Davis B. R. *et al.*, 1979, Phys. Rev. C**19**, 2259.
Declais Y. et al, 1994, Phys. Lett. **B338**, 383.
Derbin A. I. *et al.*, 1993, JETP Lett. **57**, 768.
Detwiler J., 2000, KAMLAND note 00-06, unpublished.
Eadie W. T.*et al.*, 1971, *Statistical methods of experimental physics*, (North-Holland, Amsterdam).
Eders G., 1966, Nucl. Phys. **78**, 657.
Eitel K., 2000, Nucl. Phys. Proc. Suppl. **91**, 191.
Fayans S. A., 1985, Sov. J. Nucl. Phys. **42**, 590.
Feldman G.J. and Cousins R.D., 1998, Phys. Rev. D**57**, 3873.
Fisher P., Kayser B. and McFarland K.S., 1999, Ann. Rev. Nucl. Part. Sci. **49**, 481.
Fukuda S. *et al.*, 2000, Phys. Rev. Lett. **85**, 3999.
Fukuda S. *et al.*, 2001, preprints hep-ex/0103032 and 0103033, submitted to Phys. Rev. Lett.
Fukuda Y. *et al.*, 1999, Phys. Rev. Lett. **82**, 2430.
Fukuda Y. *et al.*, 1998, Phys. Rev. Lett. **81**, 1562.
Gratta G. *et al.*, 1997, Nucl. Instr. and Meth. **A400**, 456.
Groom D.E. *et al.*, 2000, Europ. Phys. J. C**15**, 1.
Hahn A.A. *et al.*, 1989, Phys. Lett. **B218**, 365.
Harrison P.F., Perkins D.H. and Scott W.G., 1996, Phys. Lett. **B349**, 137.
James F., 1994, MINUIT Reference Manual, vers. 94.1.
Kajita T. and Totsuka Y., 2001, Rev. Mod. Phys. **73**, 85.
Kirsten T. A., 2000, Nucl. Phys. Proc. Suppl. **87**, 152.
Klapdor H-V. and Metzinger J., 1982a, Phys. Rev. Lett. **48**, 127.
Klapdor H-V. and Metzinger J., 1982b, Phys. Lett. **B112**, 22.
Kodama K. *et al.*, 2001, Phys. Lett. **B504**, 218.
Kopeikin V. I., Mikaelyan L. A., and Sinev V. V., 1997, Phys. Atom. Nucl. **60**, 172.
Y. V. Kozlov Y. V. *et al.*, 2000, Phys. Atom. Nucl. **63**, 1016.
Krauss L. *et al.*, 1984, Nature **310**, 191.
Kwon H. *et al.*, 1981, Phys. Rev. D**24**, 1097.
Llewellyn-Smith C. H., 1972, *Phys. Rep.* **3**, 261.
Maki Z., Nakagawa M., and Sakata S., 1962, Progr. Theor. Phys. **28**, 870.
Marx G., 1969, Czech. J. of Phys. B**19**, 1471.
Marx G. and Lux I., 1970, Acta Phys. Acad. Hung. **28**, 63.
Mikaelyan L., 2000, Nucl. Phys. Proc. Suppl. **91**, 120.
Mikheyev S. P. and Smirnov A. Yu., 1986a, Sov. J. Nucl. Phys. **42**, 913.
Mikheyev S. P. and Smirnov A. Yu., 1986b, Nuovo Cimento **9C**, 17.
Miller L., 2000, PhD thesis, (Stanford University).
Nicolò D., 1999, Thesis, Publication of Scuola Normale Superiore, Pisa.
Pasierb E. *et al.*, 1979, Phys. Rev. Lett. **43**, 96.
Perl M. L. *et al.*, 1975, Phys. Rev. Lett. **35**, 1489.
Piepke A. *et al.*, 1999, Nucl. Instr. and Meth. **A432**, 392.
Pontecorvo B., 1958, Sov. Phys. JETP **6**, 429.
Pontecorvo B., 1967, Zh. Eksp. Theor. Phys. **53**, 1717.
Okamura K., 1999, Ph.D. Thesis, (University of Tokyo).
Raghavan R.S. *et al.*, 1998, Phys. Rev. Lett. **80**, 635.
Reines F. and C. L. Cowan C. L., Jr., 1953, Phys. Rev. **92**, 830.
Reines F. and C. L. Cowan C. L., Jr., 1959, Phys. Rev. **113**, 273.
Reines F., Gurr H. S. , and Sobel H. W., 1976, Phys. Rev. Lett. **37**, 315.
Reines F. *et al.*, 1980, Phys. Rev. Lett. **45**, 1307.
Riley S. P. *et al.*, 1999, Phys. Rev. C **59**, 1780.
Schreckenbach K. *et al.*, 1985, Phys. Lett. **B160**,325.
Tengblad O. *et al.*, 1989, Nucl. Phys. **A503**, 136.
Vidyakin G. S. *et al.*, 1994, JETP **59**, 390.
Vogel P. *et al.*, 1981, Phys. Rev. C**24**, 1543.
Vogel P., 1984, Phys. Rev. D**29**, 1918.
Vogel P. and Engel J., 1989, Phys. Rev. D**39**, 3378.
Vogel P. and Beacom J. F., 1999, Phys. Rev. D **60**, 053003.
Wang Y-F.*et al.*, 2000, Phys. Rev. D**62**, 013012.
Wang Y-F.*et al.*, 2001, Phys. Rev. D**62**, 013012.
Wilkinson D.H., 1982, *Nucl. Phys.* **A377**, 474.
Winter K. ed., 1991, *Neutrino Physics*, (Cambridge Univ. Press, Cambridge).
Wojcicki S., 2001a, Nucl. Phys. Proc. Suppl, **91**, 216.
Wojcicki S., 2001b, talk at *Neutrino Telescopes*, Venice, March 2001, to be published in proceedings.
Wolfenstein L., 1979, Phys. Rev. D**17**, 2369.
Wolfenstein L., 1980, Phys. Rev. D**20**, 2634.
Zacek G., 1984, Dr. Thesis, (Technical University Munich).
Zacek G. *et al.*, 1986, Phys. Rev. D**34**, 2621.
Zuber K., 1998, Physics Reports **305**, 296.